PREFERENTIAL DEPOSITION OF CARBON NANOTUBES ON STAINLESS STEEL CERMET

Mohammad Samir Elassaad
Jenna Girouard
Dr. Ryan Smith

California Polytechnic State University, San Luis Obispo

June 2022

Table of Contents

1. Acknowledgements 2
2. Abstract 2
3. Introduction 2
4. Literature Review 3
    4.1. Introduction to CNTs 3
    4.2. Applications 5
    4.3. Manufacturing Methods 7
    4.4. Dispersion Fluids 9
    4.5. Steel Phases as Electromagnetic Field Concentrators 10
    4.6. Characterization 10
    4.7. Controlled Deposition Techniques for CNTs 13
5. Experimental Methods 14
    5.1. Design of Experiment 14
    5.2. Nitromax 15
    5.3. Sizing & Cutting 16
    5.4. Polishing 17
    5.5. Electrode Preparation 17
    5.6. Electrochemical Treatment 18
    5.7. Nanoparticle Mixtures 23
    5.8. Waveform Parameters 24
    5.9. Scanning Electron Microscopy 26
    5.10. Atomic Force Microscopy 27
6. Results 28
7. Discussion 38
8. Conclusions & Recommendations 39
9. References 41

1. Acknowledgements

We would like to thank Dr. Ryan T. Smith and Eric Beaton of the Materials Engineering Department, as well as Dr. Gregory E. Scott and David Robert Rodgers of the Chemistry and Biochemistry Department at California Polytechnic State University, San Luis Obispo for their contributions to this project. Dr. Ryan T. Smith conceptualized this project and supervised it throughout the year. Eric Beaton maintained department equipment necessary for this project, including the scanning electron microscope. He also checked all chemical orders and advised for safety and storage concerns. Dr. Gregory E. Scott shared with us some of his expertise on carbon nanotubes, as well as department resources. David Robert Rodgers spent a considerable amount of time with us operating the atomic force microscope to image our samples.

2. Abstract

The objective of this project is to demonstrate a method for the preferential deposition of carbon nanotubes (CNTs) on a proprietary stainless steel cermet substrate. Nitromax steels of two compositions were subject to two separate heat treatments to intentionally produce different microstructures. Samples were electrochemically passivated to isolate chromium carbide and chromium nitride island phases, which were observable in the ferric matrix surrounded by a chromium oxide film. Preferential CNT deposition on the steel surface was attempted, specifically on the chromium carbide and chromium nitride phases and boundaries. In addition to passivation, some samples were pitted to observe potential effects of corners and edges as electromagnetic field concentrators. Several types of CNTs, including those fabricated by chemical vapor deposition (CVD) and arc discharge, were tested. Variable design parameters considered included the type of nanoparticles used, dispersion fluid, surfactants, and waveform of voltage applied during deposition. The deposition of nanotubes on the surface was characterized by scanning electron microscopy (SEM) and atomic force microscopy (AFM). Waveform was found to have an effect on deposition producing unique nanostructures with various geometric, positional, conductivities, and adherence properties.

3. Introduction

Carbon nanotubes (CNTs) are a popular area of research for many applications including semiconductor technology, electrochemical storage, and x-ray emission devices. Unfortunately, controlled and efficient deposition of CNTs onto substrates has proven to be difficult to achieve, limiting the implementation of many CNT-based designs, especially for large-scale production. The objective of this project is to identify and demonstrate a method for the preferential deposition of CNTs onto Nitromax, a stainless steel cermet substrate with composition rich in carbon, chromium, and nitrogen.

This report investigates the conditions for which electrodeposition of CNTs onto Nitromax is most effective. Nitromax features a microstructure with chromium carbide and chromium nitride island phases present in amounts variable with heat treatment. These islands and their boundaries exhibit chemical and electromagnetic potentials which may attract carbon nanoparticles under certain conditions. This could allow for intentional patterning of CNTs onto the steel surface with electrodeposition, which would be useful for fabricating micro- or even nano- scaled devices. A sample preparation method was refined and design parameters were manipulated, such as the type of CNTs, dispersion fluid, surfactant, and deposition voltage waveform. If refined more with future research, the benefits of depositing nanotubes through this method could include the ability to alter deposition efficiently by heat treating the steel substrate, the ability to deposit effectively over many sites at once, and a minimally hazardous procedure for large scale fabrication.

4. Literature Review

4.1. Introduction to CNTs

CNTs are allotropes of carbon typically defined as a nanostructure formed by rolling graphene sheets into a cylindrical shape[1]. One of the major distinctions made for types of CNTs is single-walled vs. multi-walled. Single-walled carbon nanotubes (SWCNTs) are essentially sheets of monolayer graphene rolled into a tube shape. Multi-walled carbon nanotubes (MWCNTs) are essentially a series of concentric SWCNTs wrapped around each other, held together by van der Waals forces (Figure 1). Typically, SWCNTs are longer and smaller in diameter compared to MWCNTs[2]. CNTs (usually SWCNTs) with an aspect ratio such that the length is far greater than the diameter behave as nearly ideal one-dimensional (1D) nanostructures[3], [4]. 1D nanostructures are defined as having one dimension outside of the nanoscale, as opposed to 0D nanostructures, where all dimensions are nanoscale[5]. General properties of CNTs that make them desirable for a variety of applications include their high aspect ratio, high surface area, high thermal conductivity, high electrical conductivity, high tensile strength, and low thermal expansion coefficient[6].

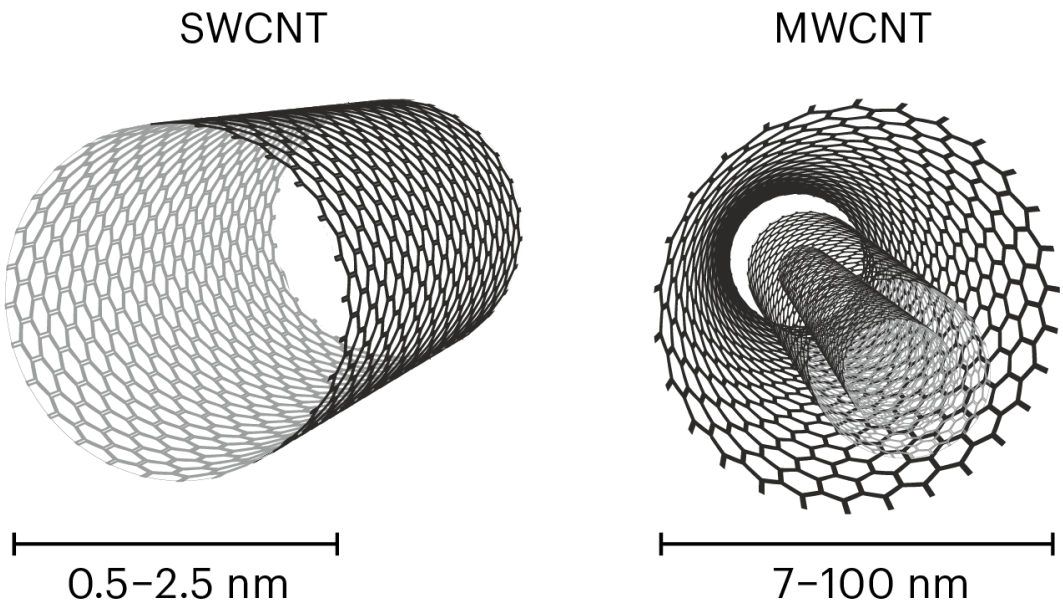

Figure 1. MWCNTs (right) are essentially a series of concentric SWCNTs (left). Typically, MWCNTs are shorter and larger in diameter compared to SWCNTs[7].

Chirality, a measure of asymmetry in the molecular structure of a CNT, is another distinction affecting its properties. The chiralities observed in CNTs are classified into three types: zig-zag (n, 0), armchair (n, n), and chiral (n, m), in which the chiral index (n, m) indicates the number of steps the carbon bonds are rotated in the hexagonal structure (Figure 2). Armchair CNTs are considered to be achiral, because n = m in this case[8]. Typically, armchair structured CNTs have a higher conductivity compared to zig-zag CNTs, which behave as semiconductors. Chiral CNTs behave as either conductors or semiconductors based on its chiral index[9].

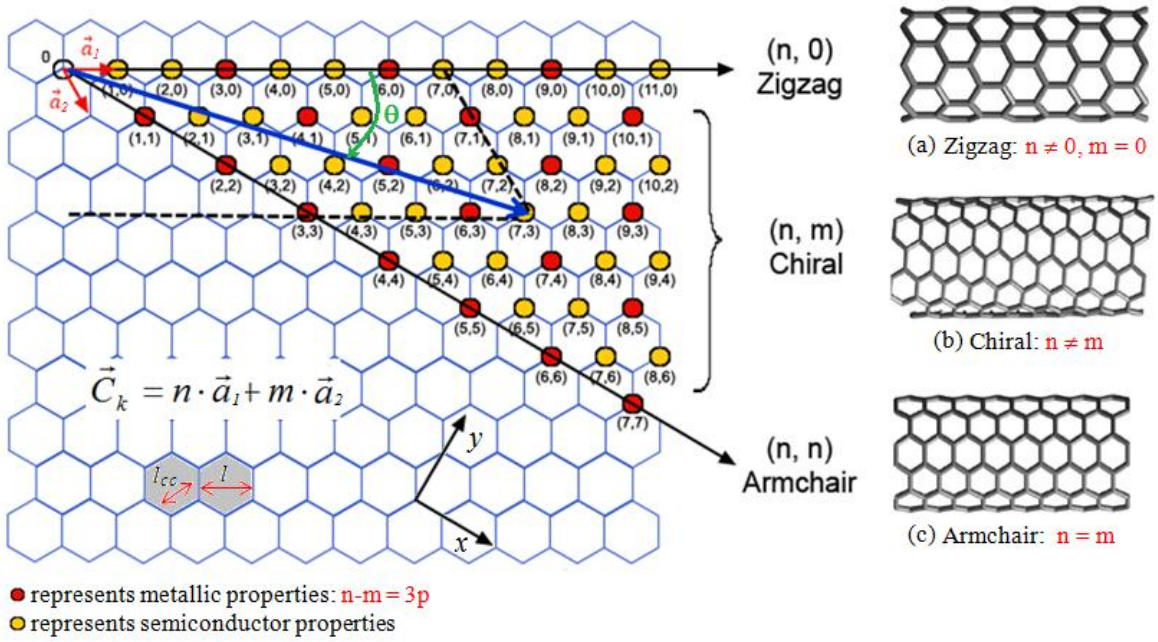

Figure 2. The chiralities of CNTs are classified into three categories based on the asymmetry of how the graphene sheets are wrapped into tubes[10].

4.2. Applications

CNTs for Improving Lithium-Ion Batteries

Graphite is currently the most common anode material for lithium-ion batteries due to its abundance, cost-efficiency, high energy density, high power density, and long cycling lifetime relative to many other anode materials[11]. However, graphite still displays a few performance limitations, including poor rate capability and dendritic formation[12]. 1D nanostructures present high surface-to-volume ratios which, when used in electrode materials, can increase the efficiency of ion exchange between electrode and electrolyte[13]. CNT modifications to both graphite and metal anodes aim to improve the efficiency, safety, and performance of lithium ion batteries by improving ion exchange while reducing volume exchange.

One of the most studied applications of CNTs for lithium-ion batteries is the incorporation or replacement of graphite with CNTs for anode materials. Some designs improve anode performance by forming a sandwich structure with CNTs surrounded by layers of graphene[14], [15]. The hollow-tube-like center of the sandwich structure works to alleviate volume change, facilitate ion exchange, and stabilize the SEI layer on cycling[16]. The reduction in volume exchange helps to prevent the formation of dendrites and reduce capacity loss over time. Better ion exchange increases the rate capabilities of the battery[17]. Many of these sandwich designs also include silicon, to improve the battery's theoretical capacity. Silicon has a theoretical capacity more than ten times greater than graphite, however silicon by itself as an

anode material results in much shorter lifetimes[18]. The incorporation of silicon in the form of composite CNTs or coatings on CNTs is an attempt to increase capacity without sacrificing lifetime[19]. Some studies have integrated CNTs into anode materials by controlled deposition via nanolithography to control porosity and pattern tortuosity at the submicron level[20].

Another method being explored for the improvement of the safety and performance of lithium-ion batteries is texturizing current collectors with lithium deposits. One way this can be achieved is with CNT or nanowire networks to guide lithium ions into pores[21], [22]. The controlled deposition of CNTs onto a current collector (commonly made of aluminum, copper, nickel, or stainless steel), could potentially help to refine the precision of this technique[23].

CNT Field-Effect Transistors

Controlling the deposition of CNTs onto a substrate aligns them relative to each other in order to get closer to their predicted hypothetical performances in applications[24]. Due to their small size, CNTs offer the opportunity to fabricate nanoelectronic devices, such as CNT field-effect transistors (CNTFETs), which are smaller than transistors achievable with silicon (Figure 3). In CNFETs, channels between the source and drain can be formed with single nanotubes or an array[25]. However, difficulties with maintaining CNT purity and precise deposition make many hypothesized designs impractical to implement[26]. So far, CNTFETs have only been fabricated in academic laboratories, and are not able to be mass produced (however many laboratories are working on solutions to this)[27].

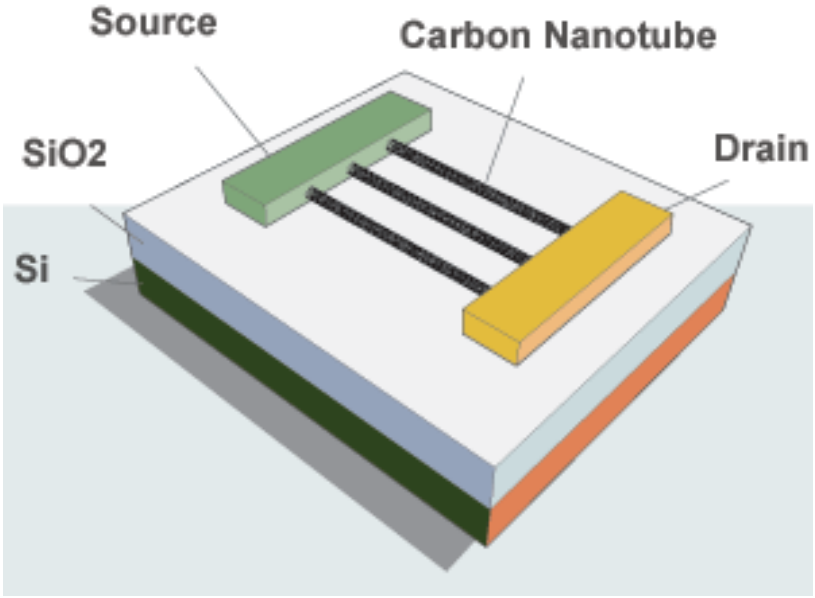

Figure 3. CNTFETs use single CNTs or an array (insead of silicon) as the channel between the source and drain[28].

4.3. Manufacturing Methods

Several techniques exist for fabricating CNTs. Properties such as diameter, length, purity and conductivity of CNTs are affected by fabrication techniques. The most common fabrication methods for CNTs are arc discharge, laser ablation, and chemical vapor deposition[29]. Arc discharge involves forming an arc plasma between two high purity graphite electrodes (Figure 4). High voltages (12-25 V) are applied in pulses to the cathode, and carbon particles are deposited on the cathode via the arc plasma as the anode is consumed. Electrode doping can be used to manipulate the properties of resulting CNTs[30]. A drawback of arc discharge CNT fabrication is that it produces other impurities, such as other carbon allotropes and irregular soot. Lower purity CNTs display less ideal properties and adherence for deposition[31]. CNT fabrication by laser ablation employs a pulsed high-powered laser to vaporize graphite in a pressurized chamber (Figure 5). Up-scaling of this technique is difficult because it requires an extremely focused laser and results in small carbon deposits. While laser ablation generally produces higher purity CNTs than arc discharge, both arc discharge and laser ablation are relatively high cost and low yield[32]. Additionally, both processes operate at temperatures greater than 1000℃[33].

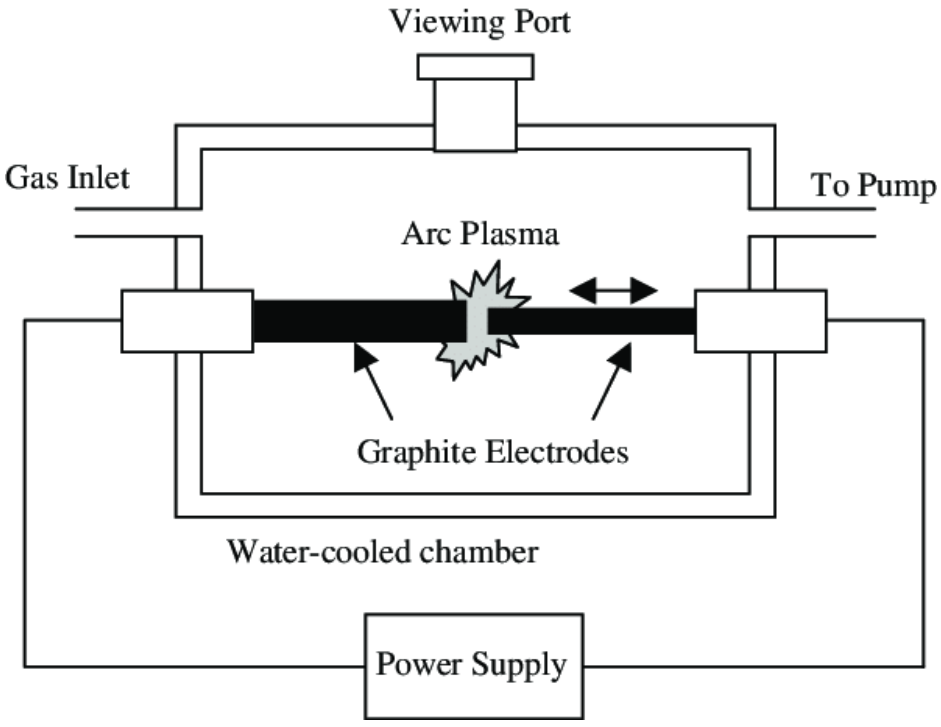

Figure 4. CNT fabrication by arc discharge involves depositing carbon nanoparticles via an arc plasma between two graphite electrodes[34].

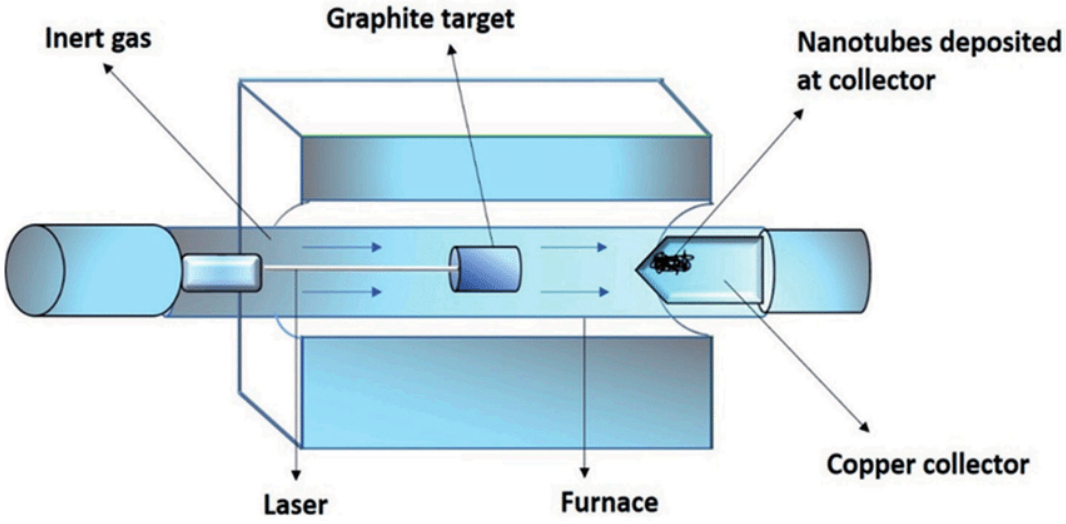

Figure 5. CNT fabrication by laser ablation involves directing a laser at a graphite target to vaporize a graphite target into nanoparticles[35].

Chemical vapor deposition (CVD) is a low cost and high yield fabrication alternative to arc discharge and laser ablation. In CVD, carbon precursors (such as CO or hydrocarbons) are heated to a gas then deposited on the surface of a nanostructured transition metal catalyst. The CNTs are then allowed to grow from that surface[36]. Figure 6 shows CVD for MWCNTs and SWCNTs. This process can occur at temperatures (600 to 1000℃) lower than arc discharge and laser ablation (approximately 1200℃)[37], [38]. The overall reaction temperature can also be lowered by starting with a gaseous or liquid carbon source. The carbon source, atmospheric chemistry, pressure, temperature, and catalyst all alter the overall geometry of the nanotubes[39]. The chemical vapor deposition process provides the opportunity for long nanotube growth times, resulting in generally longer nanotubes than those produced by arc discharge or laser ablation. CNTs fabricated with this method are also higher purity because other allotropes are not formed and they are less agglomerated[40]. For CVD fabrication with a metal catalyst, a small particle of the metal catalyst can remain in the nanotube when it is separated from the growth substrate[41]. This results in metal nanoparticle termination, a property of interest for its effect on CNT magnetism and conductivity. For the application of depositing CNTs via electrodeposition, magnetism is necessary to attract the CNTs to the electromagnetic field concentrators on the substrate.

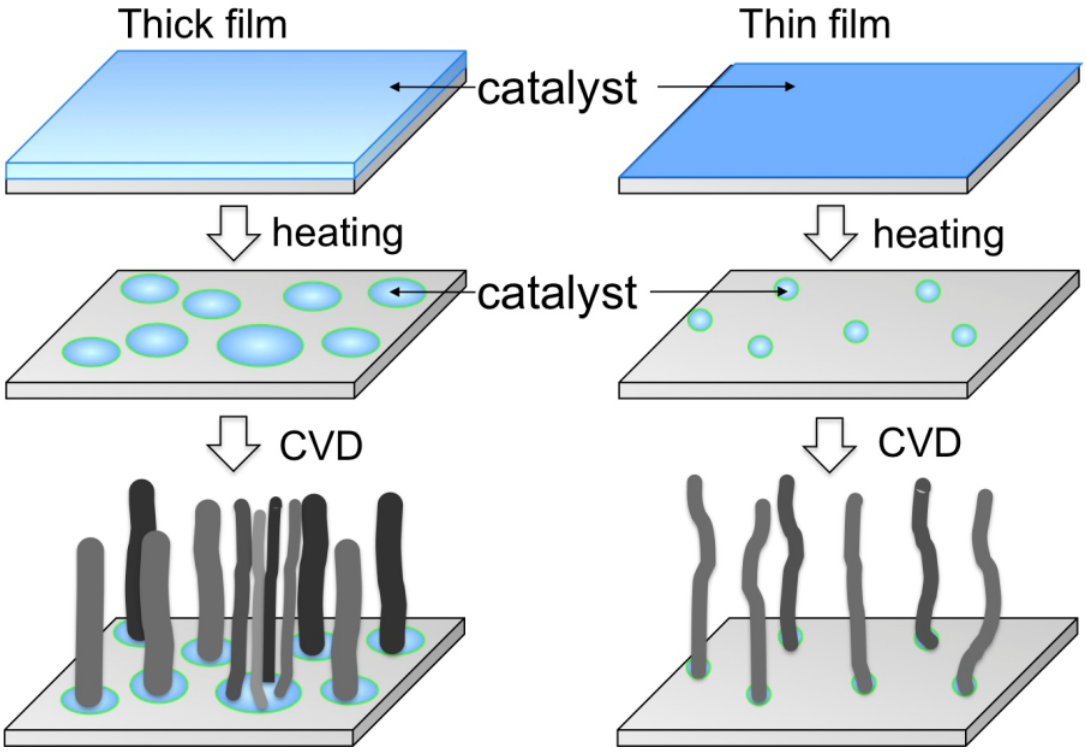

Figure 6. Fabrication by CVD involves growing CNTs onto a nanostructured catalyst from gaseous carbon[42].

4.4. Dispersion Fluids

Suspension of CNTs in a dispersion fluid is necessary for electrodeposition. Their large aspect ratio makes CNTs tend to entangle and agglomerate, making them difficult to disperse evenly in fluids[43]. Mechanical agitation, such as sonication, shear mixing, and ball milling are usually used to disperse CNTs thoroughly into the fluid, however the CNTs often do not remain in suspension for long once mixing has stopped[44]. The most common dispersion fluids for suspending CNTs are dichloroethane (DCE), tetrahydrofuran (THF), N-methyl-2-pyrrolidone (NMP), acetone, and water. DCE and THF are generally accepted as being the best performing dispersion fluids, however they are also the most hazardous to handle, store, and dispose of. Acetone has been found to perform decently in some studies and is significantly less hazardous compared to DCE and THF[45]. Because CNTs are hydrophobic, water is not an effective dispersion fluid, however it is often used out of convenience. Dispersion in water can be assisted by using a surfactant or functionalizing CNTs with acid to make them hydrophilic[46]. Octyl phenol ethoxylate and sodium dodecyl sulfate (SDS) are commonly used surfactants aid dispersion[47]. SDS encapsulates CNTs in micelles (Figure 7), reducing surface energy and entanglement, and allowing them to remain in suspension for longer periods of time[48], [43].

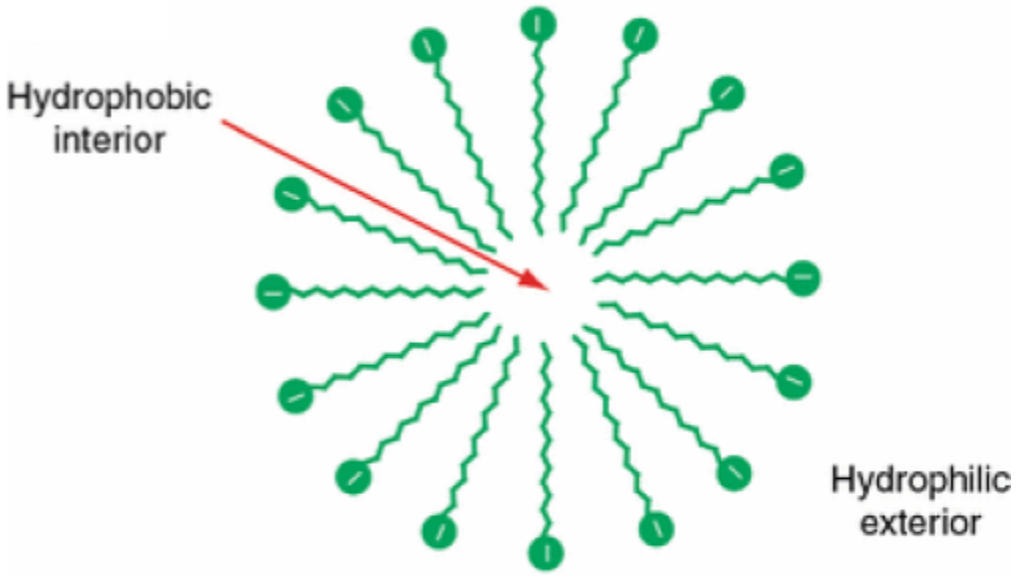

Figure 7. SDS forms a micelle with a hydrophobic interior and hydrophilic exterior[49].

4.5. Steel Phases as Electromagnetic Field Concentrators

Differences in electrical activity have been observed at grain boundaries in general for several materials[50], [51]. Even in polycrystalline materials of a single composition, the difference in crystallographic orientation between grains leads to differences in electrical activity[52]. Because of this, it is suspected that the chromium carbide and chromium nitride island phases in Nitromax not only have different electrical properties, but also thermodynamic properties than the ferric matrix. Ideally, these geometric interruptions in electronic and thermodynamic properties should behave as electromagnetic field concentrators, as they disrupt an otherwise uniform field produced by the ferric matrix. This effect may be the driving force behind the conductive CNT depositional mechanism, the result of which could produce patterned CNT structures.

4.6. Characterization

Scanning Electron Microscopy

SEM is a microscopy technique that uses electrons rather than photons to image the surface features of a sample. Due to the smaller wavelength of the particle scanning the sample surface, SEM is able to produce images with much better resolution than optical microscopy. The wavelength of optical light ranges from 400-700 nm, resulting in a minimum resolution of about 200 nm and a maximum magnification of about 1000-1500x[53]. Whereas the wavelength of electrons in SEM is about 7-40 nm (as a function of accelerating voltage), resulting in minimum

resolutions as low as 1-20 nm and a maximum magnification of about 100,000x[54], [55]. This high powered magnification is important for examining CNT depositions because it can be used to identify surface features at a much smaller scale than optical microscopy[56]. Samples suitable for analysis with SEM should be electrically conductive at the surface to limit surface charging, which results in noise and could damage the sample.

The operator-chosen settings for SEM imaging can significantly affect the quality of resulting images. A spot size of 4 nm and an accelerating voltage of 20 kV are appropriate for most applications. Increasing accelerating voltage increases the energy of the electrons scanning the sample surface, resulting in higher resolution images at a greater risk of damaging the sample. At lower accelerating voltages, there is more clarity on surface features due to the lowered interaction volume, but worse resolution[57], [58]. For imaging CNTs, a lower accelerating voltage (3 to 15 kV) may be appropriate to get more clarity of the surface features and minimize sample damage[59], [60]. Increasing the spot size (the size of the beam) at its focal point, reduces noise, but also lowers resolution. A smaller spot size can be useful for distinguishing smaller features without increasing magnification. The drawback of a smaller spot size is that the images have more noise. This can be mitigated with longer scan times, however this trade-off results in a longer process to collect images[61]. For imaging CNTs, the typical spot size of about 4 nm is appropriate, but may be adjusted as needed to achieve more clarity or noise reduction[62]. Working distance affects the focus (blurriness) of images. The beam of electrons crosses at a convergence angle proportional to the power of the electron beam after passing through the objective lens to meet at a focal point. The clearest images are produced when the physical working distance is equal to the actual working distance, based on where the focal point of the electron beam is. When the sample surface is at the focal point, images will be focused best[63]. Figure 8 shows some examples, taken of a computer chip, to demonstrate how accelerating voltage, spot size, and working distance affect imaging.

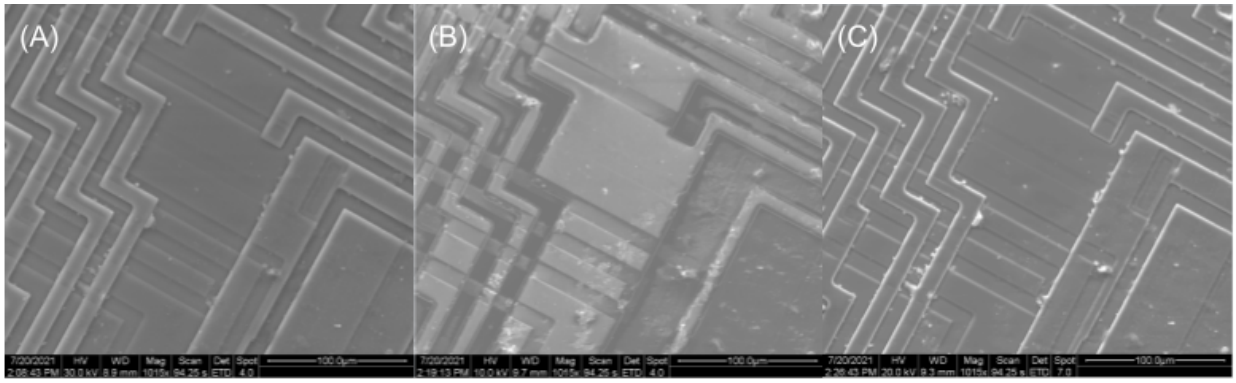

Figure 8. (A) Increasing accelerating voltage (30 kV) generally results in better image resolution, at the risk of damaging the sample. (B) Reduced accelerating voltages (10 kV) can produce images with greater differentiation of surface features. (C) Increased spot sizes (7 nm) reduce noise, but lower resolution.

Energy dispersive x-ray spectroscopy (EDS) can be used in-situ with some SEMs. EDS is useful for identifying elements present in targeted areas of a sample[64]. This would be useful for characterizing CNT deposition because it could be used to confirm that observed deposits are composed of carbon. However, this would not give information about the nanostructure of the particles, or if/how they are adhered to the substrate.

Atomic Force Microscopy

AFM is a type of scanning probe microscopy in which a cantilever tip is rastered across a sample surface to measure dispersion forces between the tip and sample. The principle components of AFM are the cantilever tip, a laser that deflects off the cantilever, a photodiode detector that detects changes in the laser angle to measure deflection of the cantilever tip, and a piezoelectric scanner that re-zeros the stage as data is collected to ensure the tip doesn't snap on the sample (Figure 9)[65]. The tip is a critical component for device functionality and performance because it determines the maximum imaging resolution achievable. Only features larger than the radius of the tip can be resolved. Dispersion forces are measured between the tip and the sample, so the smaller the tip the more sensitive to it will be to forces from smaller features. Typically, AFM tip radii are 15 nm or smaller[66].

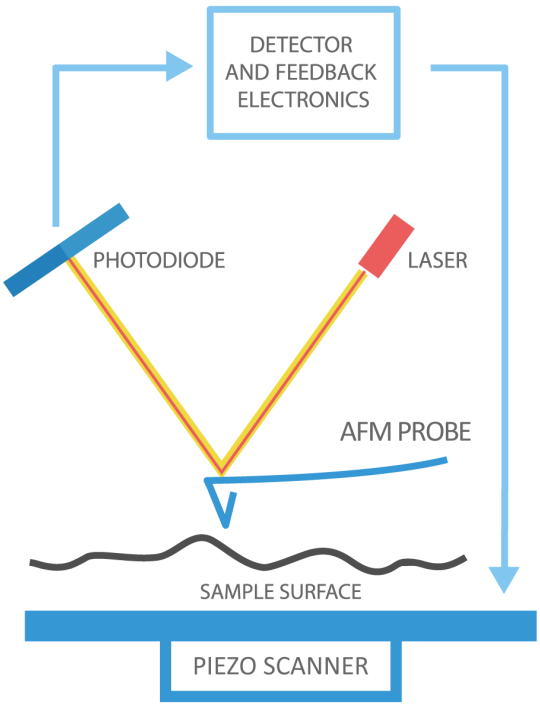

Figure 9. The main components of an AFM are shown. These components work to measure dispersion forces between the AFM probe tip and the sample surface[67].

Three imaging modes (contact, tapping, and non-contact), related to the amount of contact the tip makes with the sample, exist for AFM. While contact mode is generally easiest to perform, tapping and non-contact modes are better suited for soft or otherwise delicate samples because the physical dragging that occurs in contact mode may damage them[68]. In non-contact mode, the tip never touches the sample surface, operating under a slightly attractive regime. The tip is kept an order of 10 nm away from the sample and oscillated at a resonant frequency to image the surface. This is better for softer samples, however it is not as sensitive as contact mode, so smaller features on the sample may be more difficult to detect. Tapping mode combines the contact and non-contact modes by intermittently tapping the sample with the tip[69], [70]. Non-contact or tapping modes are preferable for characterizing CNTs to minimize damage to the carbon structures.

4.7. Controlled Deposition Techniques for CNTs

The most common of the few existing methods for patterning CNTs onto a substrate is by using nanolithography to pattern a substrate. Conventional electron-beam lithography with a polymethyl methacrylate (PMMA) mask is used to pattern a catalyst onto a substrate for CVD. This can achieve nanoscale patterning[71]. One of the major drawbacks of this technique is that it requires expensive, high maintenance equipment. Additionally, it requires the growth of CNTs directly onto a substrate, rather than the option to deposit already grown CNTs. AFM nanolithography has been used to chemically pattern substrates for deposition of dispersed CNTs. Amino-functionalized surfaces may affect the adherence of SWCNTs, allowing for precision chemical patterning with nanolithography followed by physical deposition or electrodeposition[72], [73].

Electrodeposition is the deposition method of interest for this project. While this deposition method is controlled in the sense that it can be used to align CNTs on the electrode surface, the “patterning” is coming from the suspected electromagnetic field concentrators in the substrate microstructure. The general principle of electrodeposition, or electrophoretic deposition (EPD), is that charged particles suspended in a dispersion fluid will move toward an anode (or cathode in cathodic EPD) in the presence of a voltage. The setup is similar to an electrochemical cell, with an anode, cathothode, reference electrode, and power supply (Figure 10). However, it is different from an electrochemical cell, because the intention is not to induce any reactions at the electrodes, but only to use the electric field to guide the charged particles toward the anode. Initial research on depositions this way focused on applying DC voltage, however more recent research has interest in AC voltages and varying waveforms[74], [75], [76].

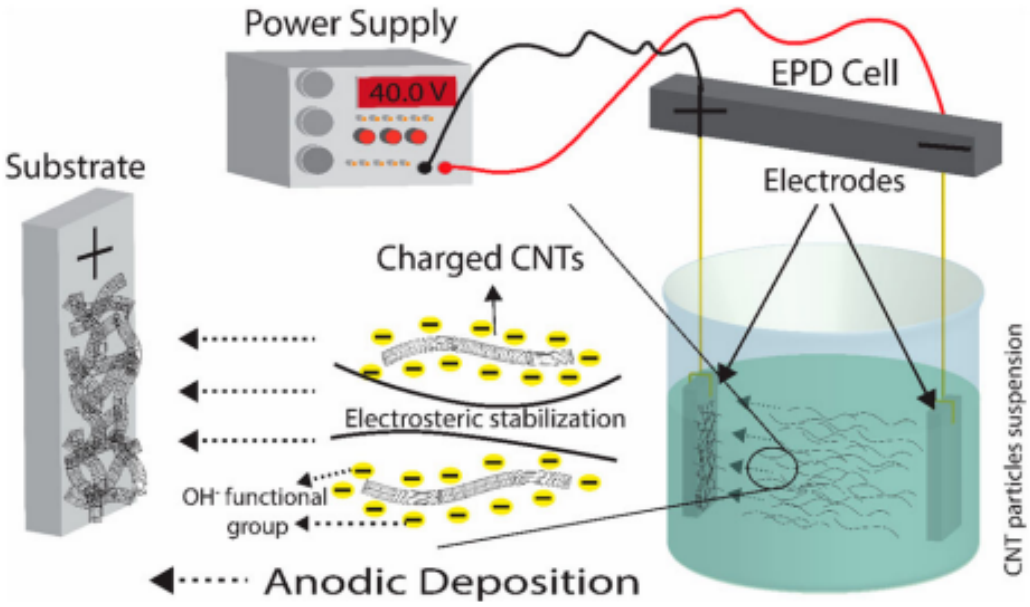

Figure 10. Electrodeposition with an EPD uses an electromagnetic field to guide CNTs towards the anode[74].

5. Experimental Methods

5.1. Design of Experiment

The objective of this project is to preferentially deposit metal-nanoparticle-terminated SWCNTs onto a passivated stainless steel substrate. However, the testing parameters and variables of this project evolved over its run. Not only are CNTs physically difficult to manipulate, but the mechanisms of some of their properties are still debated. For these reasons, this project focused more on experimental ideas rather than data collection. Nonetheless, primary benchmarks were still developed for future studies to collect data with scientific significance and repeatability. Specifically, elecrochemically passivated proprietary stainless steel samples were subjected to various depositional environments. The variables under comparison were CNTs in dispersion fluids and applied electromagnetic fields (varying by potentiodynamic waveform). Table 1 organizes the details of the experimental setup. Characterization of results was done with SEM and AFM.

Table 1.

Applied Electromagnetic Field Potentiodynamic Waveform						
CNT Dispersion Fluids		Physical	Linear Sweep	Potential Step	Cyclic Square	Power Pulses
	Tuball + DMS	X	✓	X	X	X
	Arc + H2O + IPA	✓	✓	✓	✓	✓
	CVD + SDS + Acetone	✓	✓	✓	✓	✓

5.2. Nitromax

Two compositions of Nitromax at two heat treatments were prepared to demonstrate how the microstructure can be varied by adjusting these parameters. However, composition and heat treatment were not considered later as variables impacting the effectiveness of CNT deposition. This is because it is suspected that composition and heat treatment only affect the location and ubiquity of chromium carbide and nitride phases, and not the electrochemical properties of the phases. The general composition of Nitromax is shown in Table 2. Nitrogen content is the main difference between the two compositions used in this study, nicknamed H52 and H48. Several Nitromax ingots of each composition were heat treated in an electric furnace at either 1050℃ or 1200℃, then allowed to air cool to room temperature.

Table 2. Composition of Nitromax Steel Cermet

Element	**Content (wt. %)**
Chromium	28 - 30
Nickel	2 - 4
Carbon	1.7 - 2.2
Manganese	1 - 2

Molybdenum	1 - 1.5
Phosphorus	< 0.005
Sulfur	< 0.001
Nitrogen	0.35 - 0.38* 0.44**

*H52 composition **H48 composition

5.3. Sizing & Cutting

Heat treated Nitromax ingots were acquired as rectangular blocks 1.25 cm in width, 1.5 cm in height, and 4 cm in length. The ingots were sectioned into smaller working prisms with thickness of 0.25 cm, with a testing surface area of 1.875 cm^2. Figure 11 conveys the dimensions of the source material and the working sample sizes. A Tech Cut 4 precision low speed saw was used with a high concentration 5 in x 0.015 in x 0.5 in diamond metal bonded wafering blade (ID# 60-20075). Allied High Tech Products Incorporated also supplied low speed cutting fluid (ID# 60-20115) to lubricate the set and keep the blade mobile, preventing lodges, warping, and disc breakage. Nitromax is an extremely hard alloy, making it difficult to cut. Each ingot was angled in the vice grips so the first point of contact by the diamond saw would be at a corner. Once the blade passed half way through the diagonal cross section, the source ingot was rotated about its longitudinal axis to cut into the corner opposite, while maintaining alignment with the first half pass. Approximately 24 hours were required for one diagonal half pass, making the total cutting time to produce each working sample approximately 48 hours. Eight total samples were cut.

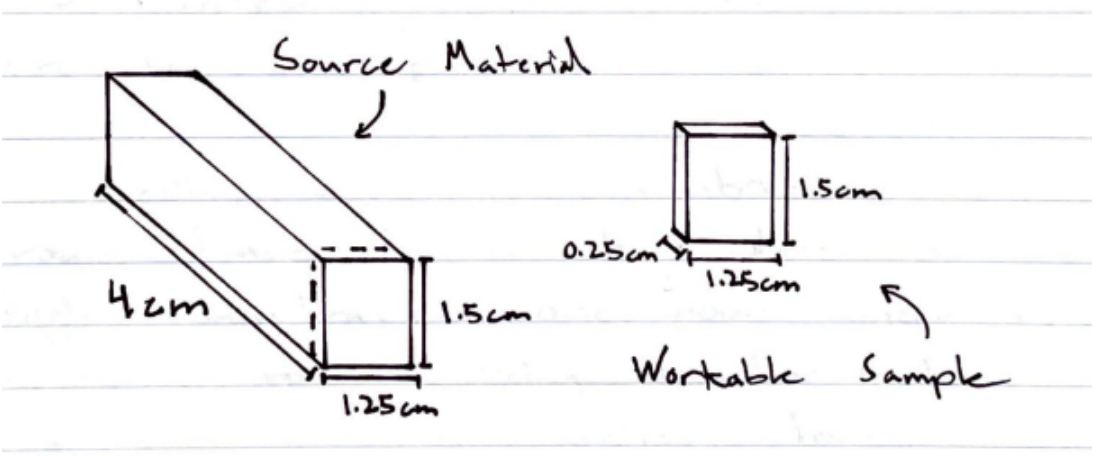

Figure 11. The dimensions of a Nitromax ingot and a working sample sectioned from it are shown.

5.4. Polishing

Next, one of the 1.5 cm x 1.25 cm surfaces on each of the working samples was grinded individually to an even finish on sanding tables. Sanding paper was wet with distilled water and samples were moved only in one direction (as opposed to back and forth) on each paper. The order of sanding paper is chronological as follows: 240, 320, 400, 600 (grit). Samples were turned 90◦ between each paper to ensure all scratches from the previous paper were removed before continuing. After grinding, four Allied M-Prep 5 Polishing Machines were used to polish the samples to a 0.05 µm finish. For the first three pads, diamond spray was applied with abrasive particles sized as follows: 6 µm, 3 µm, and 1 µm. For the finest pad, an aluminum oxide (Al_2O_3) and cerium (IV) oxide (CeO_2) liquid with 0.05 µm particle size was applied. All pads were rotating at 250 RPM and a non-abrasive lubricant (composed of 80% water, 10% ethylene glycol, and 10% methanol) was applied. Washing and drying of hands and samples was done repeatedly throughout polishing in order to prevent contamination of any polishing pads.

5.5. Electrode Preparation

After polishing, each metal sample was converted into an electrode for an electrochemical cell. First, a small rectangular surface was abraded onto the backside (the side opposite the polished side) of each sample using a Dremel Lite Tool (ID# 776-N/10) tipped with a green course grinding bit (ID# 83142). This was done to expose fresh unoxidized metal that a chromel wire could be welded to. Figure 12 conveys a diagram of this abrasion. Chromel P thermocouple wire from Hoskins MFG CO Detroit (ID# C6371) was pressed onto the newly exposed area with copper electrodes. The wire was then spot welded in place with a Kerpu machine in the presence of a borax flux. Next, the chromel was then cut to a length of about 40 centimeters to include sufficient sink depth, metallic connection, and slack. Finally, to avoid treating or testing unwanted surfaces, rears, corners, edges, and the majority of the wire was insulated with Gardner Bender Green Liquid Waterproof Electrical Tape. Figure 13 displays a completed electrode alongside the materials required to craft this item.

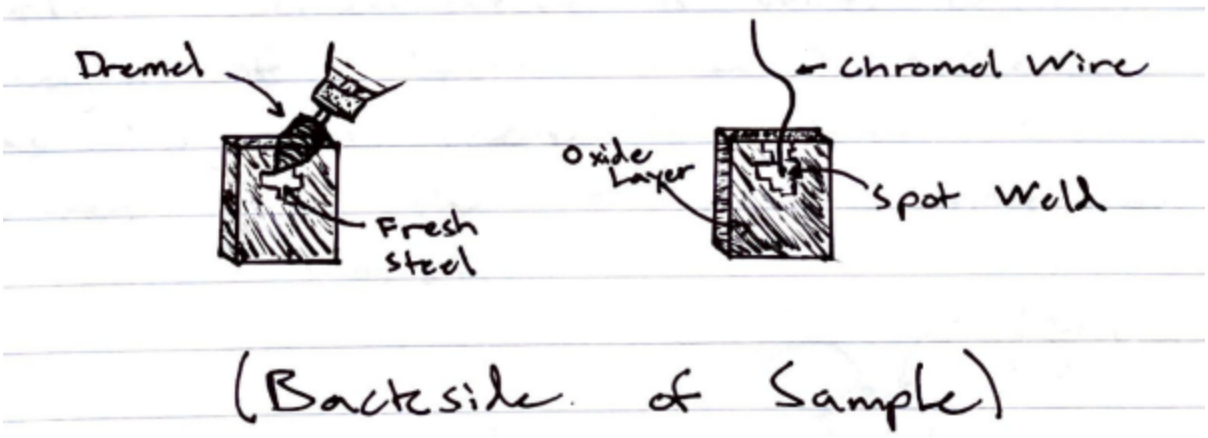

Figure 12. A dremel tool was used to expose unoxidized steel and a chromel wire was spot welded to the backside of each sample.

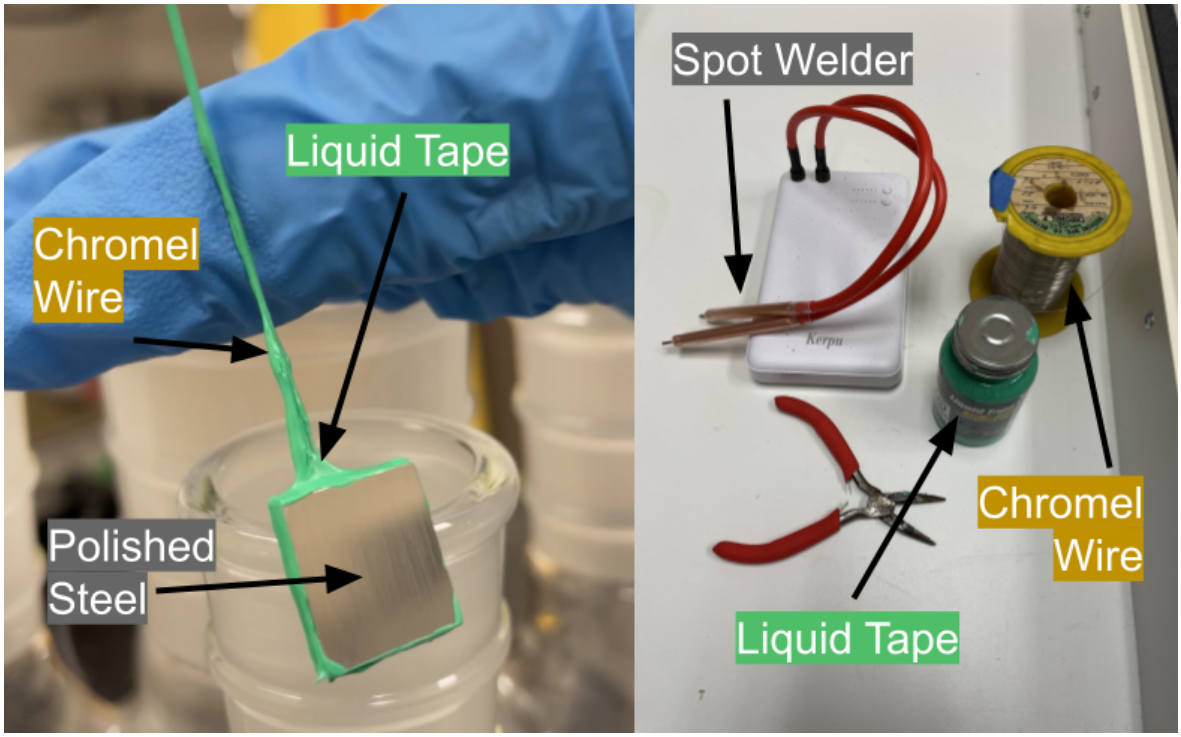

Figure 13. Liquid tape was applied to cover all surfaces other than the polished test surface, including the chromel wire spot welded to the backside.

5.6. Electrochemical Treatment

Before nanotubes can be deposited on electrodes, the surface must be electrochemically treated. The goal of passivating is to form an electrically insulating and chemically noble chromium oxide layer (Cr_2O_3) on top of the ferric matrix, surrounding the chromium carbide and

nitride islands, but not covering them. The growth of this oxide layer is spontaneous but can be further induced through a contaminant cleaning process called passivation, defined by ASTM A380 and A967[77], [78].

There are countless methods to passivate stainless steels through different oxidizing solutions and electrical impulses. For the purposes of this experiment, 1 L of a simple 1 M H_2SO_4 electrolyte was derived from 20 wt.% sulfuric acid (Ricca Chemical Company + Cat. No. 8166-1). The electrolyte was poured into a glass container submerging a triple electrode setup. The stainless steel sample is identified as the working electrode. A platinum coated wire mesh served as a counter electrode (to complete the electrochemical cell). Last, a saturated calomel (mercury and potassium chloride Hg_2Cl_2 + KCl) reference electrode (manufactured by Princeton Applied Research and distributed through Koslow Scientific Company) was used to measure relative voltage and current data. The triple electrode setup was connected to a Parstat 2273 Advanced Electrochemical System by Princeton Applied Research as well as a computer.

Once an electrochemical cell is established, the treatment can begin. Linear sweeps were conducted with the AM316L template starting at -0.75 V gradually rising to 1 V with a sweep rate of 0.6 V/min. Ideally, the linear sweep rate of a potentiodynamic test should be 0.6 V/hour as stated by ASTM G5[79]. However, the goal of this treatment is not to establish statistical significance for corrosion behaviors,but simply to form the passivation layer, so a rapid rate will suffice. The primary reason a linear sweep was chosen over a constant applied voltage for a certain time is due to the variation in steel compositions and heat treatments. These characteristics might have an affect on the corrosion, passivation, and trans passivation potentials. In order to avoid these deviations, linear sweeps were done to constantly monitor the relationship between voltage and current for each individual sample during its own electrochemical treatment.

The treatment started with a negative applied voltage, making the sample working electrode act as a cathode producing hydrogen bubbles at its surface while the platinum counter electrode behaves as an anode producing oxygen bubbles. This is known as the cathodic reaction where electrolysis occurs. As the voltage becomes more positive, the rate of the cathodic reaction decreases until the corrosion potential (E_{corr}). At this voltage, current is at its lowest, and the cathodic reaction shifts into the anodic reaction, switching the charges on each electrode. The working sample electrode becomes the anode and the platinum counter electrode becomes the cathode.

As voltage continues to rise in the positive direction, current begins to copy. This is the result of metal activation, where ferric ions (Fe^{2+}) detach from the working sample anode and travel towards the platinum counter cathode. However, the platinum cathode is chemically noble, so the ferric ions, rather than attach themselves to the cathode surface, are lost in the electrolyte solution. This kind of reaction is typical of most electroplating processes (excluding the nobility of the cathode) and continues until current starts to drop once more.

When the current starts to drop again with increasing voltage, passivation begins. The metal surface has been readily cleaned from debris and the chromium oxide (Cr_2O_3) starts to form. Although the ferric matrix is mostly iron, it is also heavily alloyed with chromium and other elements. This is why the matrix background itself possesses the ability to spontaneously construct a passivation layer. The insoluble chromium oxide passivation layer is electrically insulative and prevents active corrosion. The metal matrix itself becomes immune while highlighting the chromium carbide and nitride islands as electromagnetic field concentrators. This is why the current continues to decrease as the oxide layer thickens. Once current stabilizes and then reaches another turning point, the passivation layer has finished developing. For the preparation of nanotube depositional surfaces, this point in the electrochemical treatment sufficed and the linear sweep was terminated. Figure 14 conveys the difference between an untreated and an electrochemically passivated steel surface at similar magnifications.

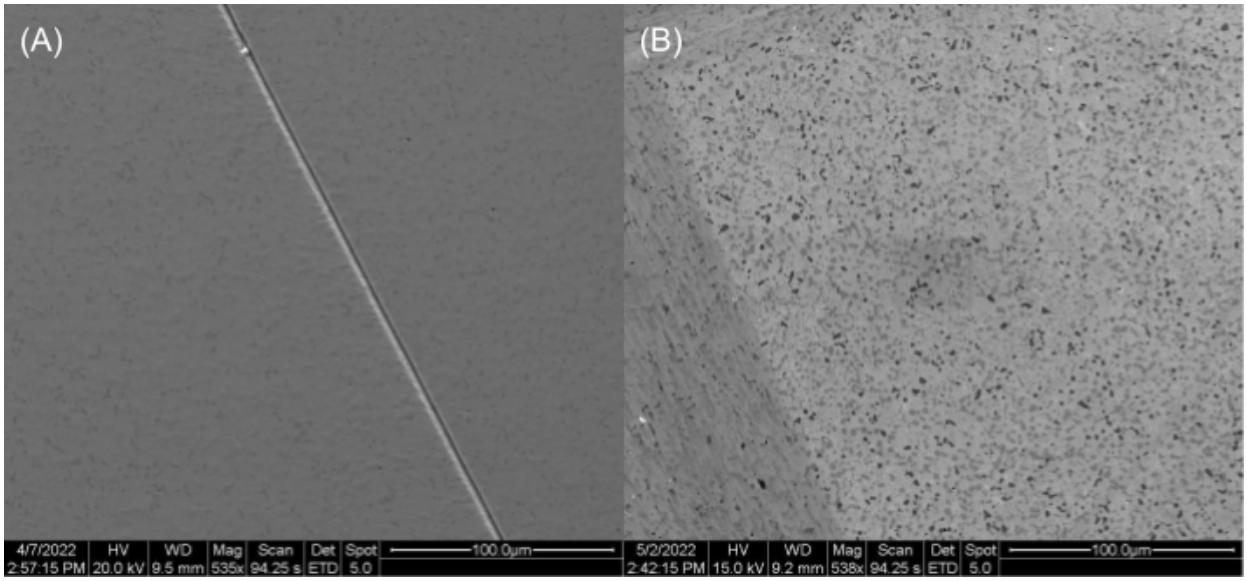

Figure 14. The effect of passivation can be derived from these captures. (A) This stainless steel surface has been super polished down to 0.05 micron precision. (B) The white chromium oxide film exposes the chromium carbide and nitride microstructure after the passivation electrochemical treatment.

However, if the voltage were to continue rising, the curve would enter the transpassive region. In this zone, the applied electrical potential is large enough to induce pitting corrosion, an autocatalytic process. The boundaries of the ferric matrix are dissolved and bond with the sulfuric acid to form ferric sulfates ($Fe_2[SO_4]_3$). This weakens the surrounding structure holding the chromium carbide and nitride islands, causing them to fall out of the matrix. The resulting holes become primary areas for pitting corrosion to occur, producing more and more ferric sulfates. This kind of corrosion is the most damaging to the metal surface. However, there is a possibility that the new surface full of corners, edges, and cusps, may highlight different electromagnetic field concentrators. Figure 15 displays the comparison between an

electrochemically passivated surface and an overtreated chemically pitted surface. Figure 16 illustrates the linear sweeps associated with individual electrochemical treatments while Figure 17 presents a more indepth schematic.

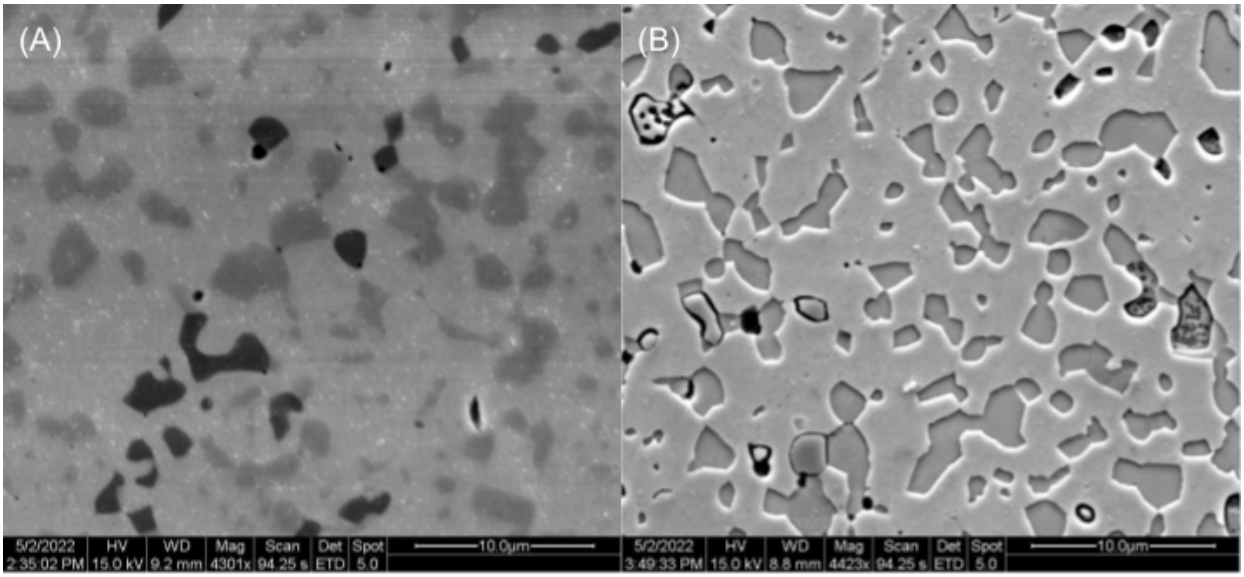

Figure 15. Above are micrographs that show the difference between a passivated and a pitted stainless steel surface. (A) This is an ideal surface prepped and ready for nanotube deposition. (B) This sample suffered prolonged exposure to the electrochemical treatment. The chromium carbide and nitride phase have either fallen out of the matrix or were disintegrated. If left even longer in the electrolyte, deeper wells will occur due to the autocatalytic nature of pitting corrosion.

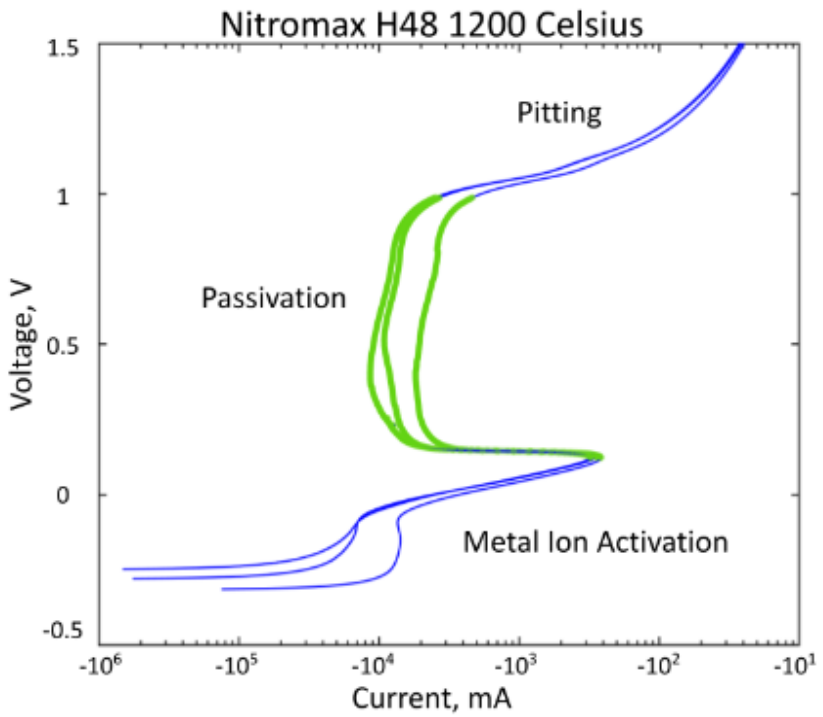

Figure 16. This graph conveys voltage versus current for the electrochemical passivation process of some stainless steel nitromax samples. Ideally, the treatment would end at the positive edge of the green zone.

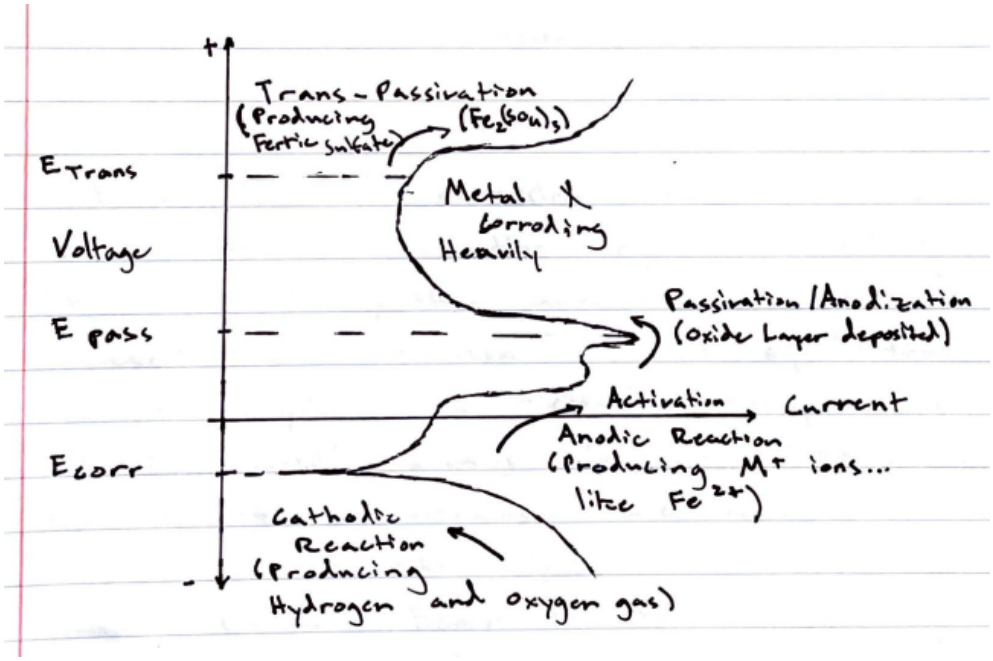

Figure 17. A drawn schematic of the electrochemical linear sweep treating stainless steel. Distinct sections of the voltage current curve represent isolated chemical reactions and electrical potentials.

5.7. Nanoparticle Mixtures

Two types of CNTs were considered for this experiment. The main difference between these two types is the process by which they were manufactured, arc discharge or chemical vapor deposition (CVD). A third type, Tuball battery NMP CNTs, was initially considered. These CNTs came already suspended in a 1-methyl-2-pyrrolidone (NMP) and 1,1 difluoroethylene polymer dispersion fluid. However, this dispersion fluid was too thick for electrodeposition. An attempt was made to dissolve the 1,1 difluoroethylene with dimethyl sulfoxide (DMSO) to allow the suspension fluid to break apart and be diluted with water or phosphoric acid. Despite this, these CNTs proved significantly more difficult to disperse compared to the other two types and were abandoned early on.

Several dispersion fluids were considered in this experiment. DCE and THF are two of the most commonly used dispersion fluids for CNTs. However, since this project is focusing on finding deposition methods that would be suitable for larger scale production, DCE and THF were not considered due to the significant safety risks they pose. Instead water, isopropyl alcohol (IPA), sulfuric acid, phosphoric acid, and acetone were considered. The acetone dispersion fluid included SDS, a common detergent, to act as a surfactant. All other dispersion fluids did not include surfactants, however IPA is often considered a surfactant.

CNTs were either deposited in a separate step after the passivation in sulfuric acid, or they were passivated and deposited in a single step. For the CNTs that were deposited with sulfuric acid, this was done in one single step with the passivation. CNTs dispersed in water, IPA, or acetone with SDS were deposited in a step separate from passivation. All CNTs were ultrasonicated, with a Qsonica sonicator, into suspension for approximately 15 minutes at intervals of one second on and one second off. Table 3 shows the concentration of CNTs tested in each dispersion fluid.

Table 3. CNT Concentrations in Dispersion Fluids

Dispersion Fluid	CNT Type	CNT Concentration (mg/L)
Water	Arc Discharge	1.285
Sulfuric Acid	Arc Discharge	1.285
IPA	Arc Discharge	1.285
Phosphoric Acid	Tuball NMP + DMSO	1.285
Acetone + SDS*	CVD	50 mg/L

*SDS Concentration 0.733 mg/L

5.8. Waveform Parameters

The Parstat 2273 Advanced Electrochemical System developed by Princeton Applied Research is capable of many electrical processes. To capture the relationship between electrical stimulus and CNT deposition, several waveforms were tested. These waveforms primarily differed in timing, rather than large differences in voltage amplitude. This was done to reduce the altering variables of the experiment. Specifically, five depositional methods were conducted, physical, linear sweep, potential step, cyclic square wave, and power pulses, all of which are individual templates in the Parstat Star E software.

Physical deposition involved simply dropping a drop of liquid mixture onto the sample surface and allowing it to evaporate. This helped determine a baseline for comparison between electrically stimulated and unstimulated samples. Linear sweeps started at -0.75 V and gradually rose to +1 V with a sweep rate of 10mV/s. This waveform is identical to the one used for electrochemical treatment. Potential steps applied a constant +300 mV for 300 seconds. Cyclic square waves altered between -1 V and +1 V potential steps lasting 3 seconds each for a total of 300 seconds. Finally, power pulses involved a similar pattern to cyclic square waves, with more steps and less time in between each step. Specifically, the waveform starts with a +1 V step for 0.5 seconds, followed by a 0.25 second break, then a +0.5 V step for 0.35 seconds. Then the negative clone of these amplitudes are applied, with the following round alternating back to positive. These pulses are repeated for a total of 300 seconds as well. Figure 18 depicts each waveform and its identifying characteristics, and Figure 19 show graphs of collected data.

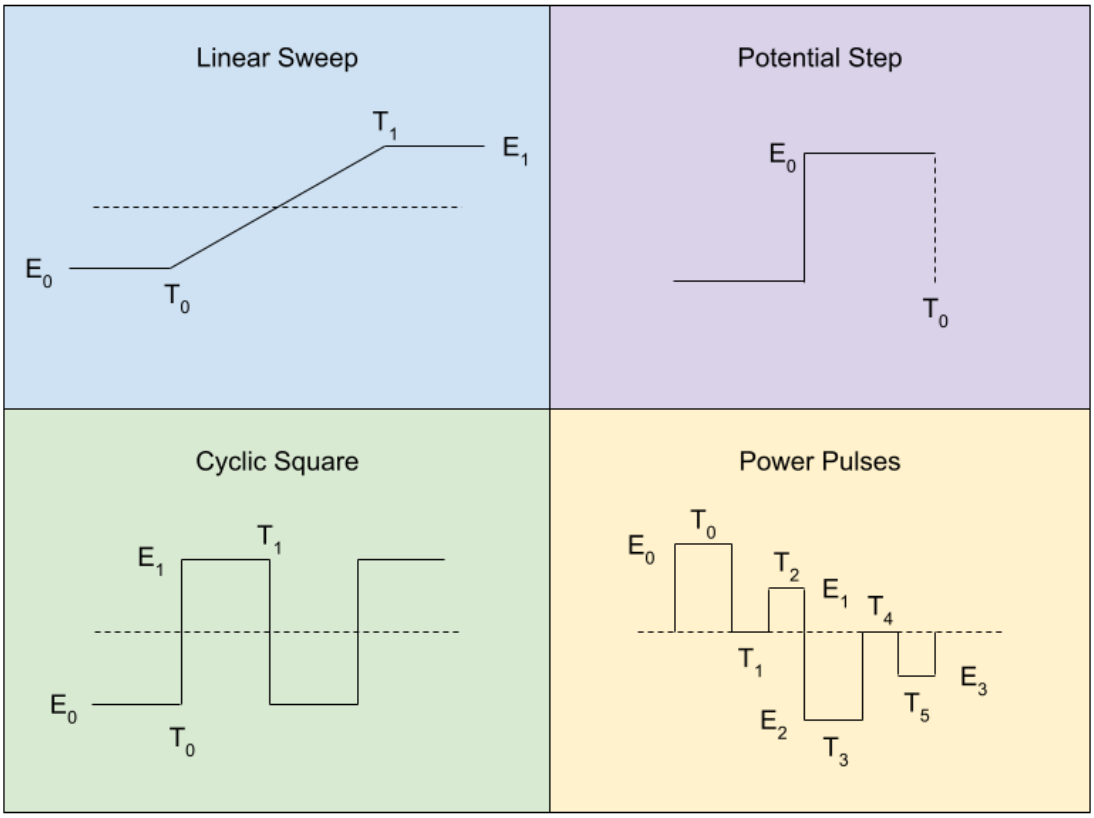

Figure 18. These diagrams provide good visual representations of the variant waveforms applied to alter nanoparticle deposition. The letter E with subscripts signifies unique voltages. The letter T with subscripts identifies certain time frames. It is important to note that cyclic square and power pulses waveforms alternate between positive and negative voltages consistently.

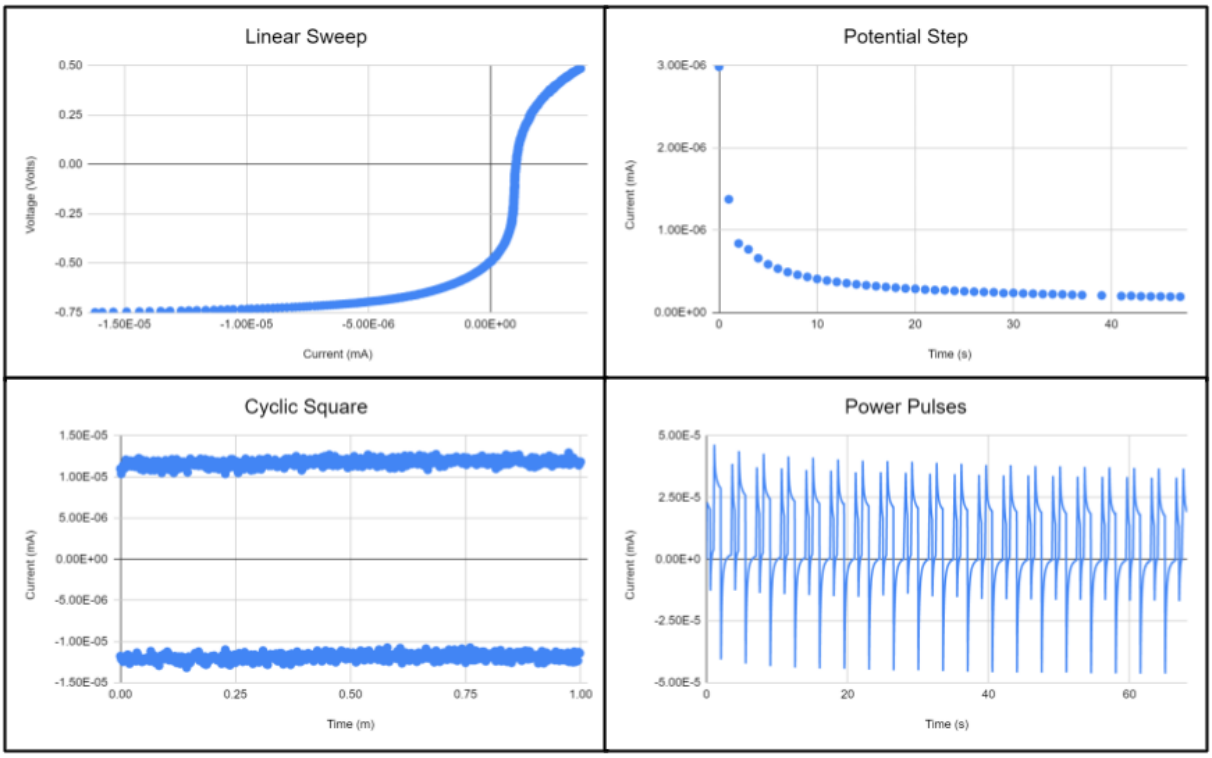

Figure 19. These graphs showcase typical electrical data collection during the nanotube deposition process. Although they are not necessarily relevant to the scope of this project, this data can still be useful to ensure proper waveforms, voltages, currents, and times are being applied.

5.9. Scanning Electron Microscopy

SEM micrographs were taken at various stages of the project by a Fei Quanta 200, including after rough polishing, after super polishing, after passivation, and after deposition. Masking tape labels were removed from samples (but samples were tracked) before putting them into the SEM to prevent contamination of the chamber and column. Double-sided carbon tape was used to secure the samples to sample holders. Carbon tape is usually used with the SEM, because it is conductive, to maintain a path to ground. However, in this case it is not particularly necessary that the tape be conductive because it was adhered to the insulating liquid tape on the back of the sample. The path to ground was instead established by wrapping the electrode wire around the base of the sample holder.

Before imaging was finished, the SEM in the materials engineering department started having difficulties focussing, likely due to a contaminated column that could not be repaired within the timeline of this project. The SEM micrographs taken after this technical difficulty were imaged with the biomedical engineering department's clean room SEM. This is why the marker bars look different on some of the micrographs. Samples imaged on the SEM in the clean room were disassembled from the electrode entirely to be extra careful to prevent contamination in the clean room.

The information bars on the bottom of the SEM images (taken the materials engineering department) display the date and time the image was captured, vacuum mode (high or low), working distance (distance between the sample surface and objective lens), scanning rate of the electron beam, detector used, spot size (diameter of the electron beam), accelerating voltage, and a marker bar. The information bars on the images from the clean room SEM include less details, but the most important information (magnification and marker bar) is included. The information bar on each SEM image shows the exact magnification, but most of the images taken are at about 5000x or below. Magnifications were chosen based on whatever magnification best showed the features of interest for each particular sample. High vacuum mode was used because the samples were conductive. A spot size of 5.0 was chosen to minimize noise, and an accelerating voltage of 15.0 kV was chosen to maximize resolution without damaging the samples. However, some surface burning did occur due to prolonged exposure to the electron beam.

5.10. Atomic Force Microscopy

An Asylum MFP-3D AFM was used to collect additional data on some samples. A sample with arc discharged CNTs passivated and deposited in a single step linear sweep, and a sample passivated then physically deposited with CVD CNTs were characterized with AFM. Images were taken with a 7 nm silicon cantilever tip. Non-contact mode was used to avoid damaging sample surfaces. Electrodes were disassembled to ensure the steel could lay flat in the AFM. Lateral resolution for these images is on the order of a few microns. The height resolution is on the order of 50-200 nm. Images were analyzed with Gwyddion visualization software.

6. Results

The SEM and AFM micrographs collected of the steel surfaces after CNT deposition are shown in Figures 20 through 31 below.

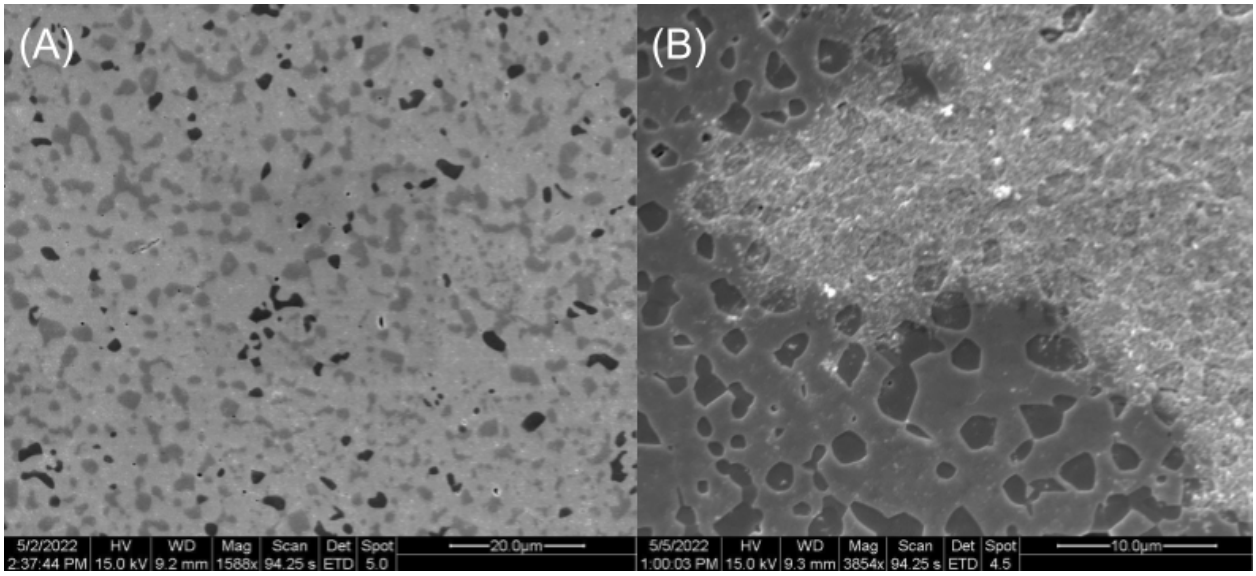

Figure 20. (A) This is an ideal passivated stainless steel surface. Chromium carbide and nitride islands can be seen piercing out of the lighter ferric matrix. The darker islands are nitrides while the lighter islands are carbides. (B) This sample has been over-treated both electrochemically and with an unnecessarily high nanotube concentration. A nanotube forest can be seen blanketing the microstructure.

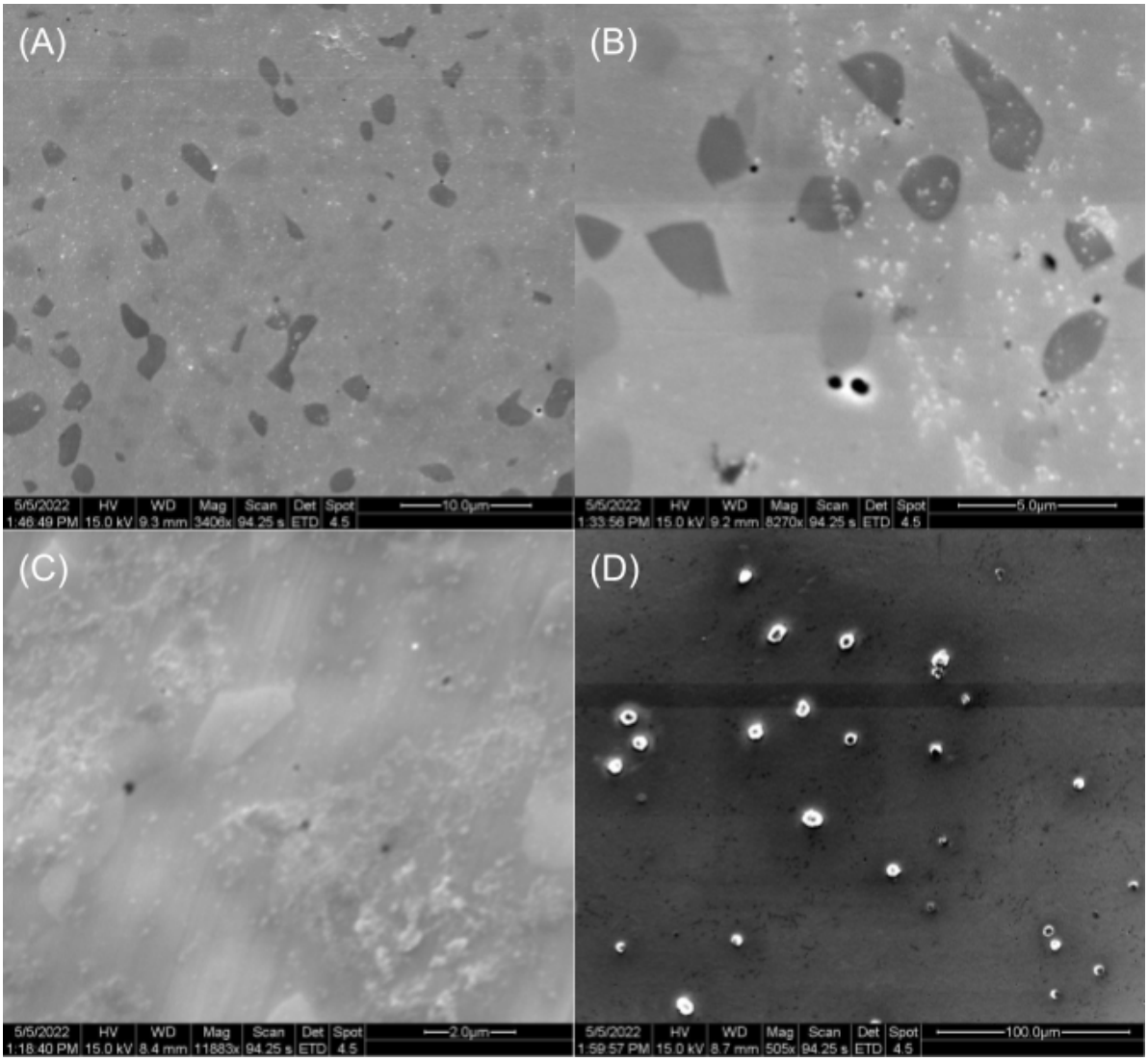

Figure 21. Above are the depositions involving separate sulfuric acid passivation and nanotube depositional treatments for a multistep program. The nanotube mixture primarily contained isopropyl alcohol and arc discharge nanotubes. (A) The linear sweep application deposited little nanoparticles. (B) The potential step deposition deposited particles that would hug the edges of liquid drops. (C) The cyclic square wave randomly dispersed clouds of nanoparticles. (D) The power pulses spheroidized the nanoparticles into ball like aggregates atop the steel surface. These spheres did not adhere well and were less conductive as can be seen by their bright appearance in the SEM.

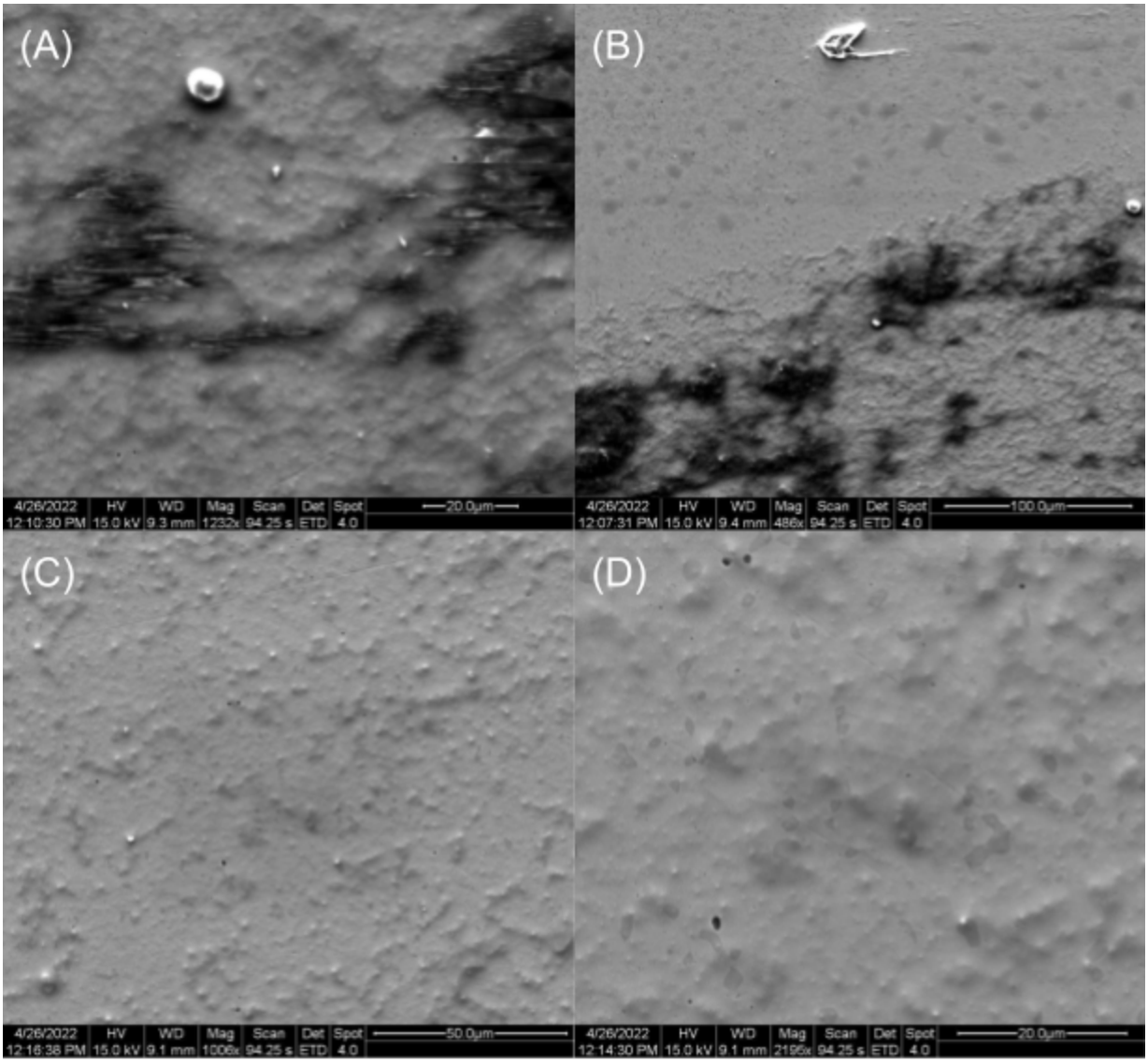

Figure 22. These micrographs convey a single step process that included Tuball BATT NMP nanotubes, phosphoric acid, and dimethyl sulfoxide. (A) Nanotubes can be seen still trapped in a liquid film. (B) The boundary between nanotubes in a film and a dryer surface on the steel. (C) Dust particles can be seen underneath an unevaporated film of nanotube and phosphoric electrolyte. (D) The passivation result is different and less effective with phosphoric acid.

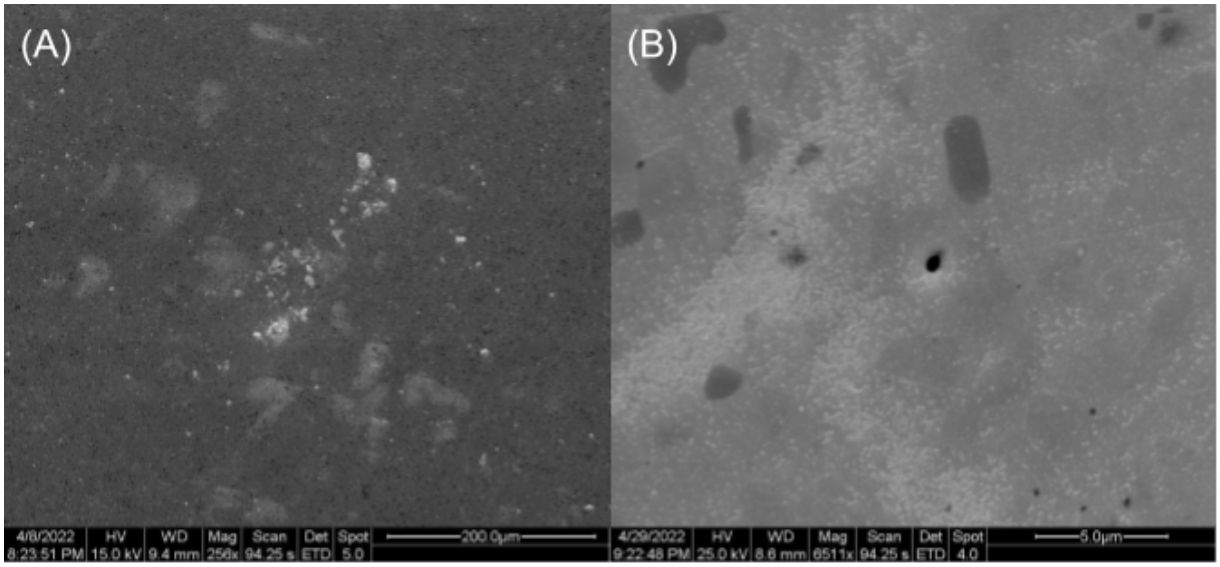

Figure 23. Above are simple test depositions conducted with arc nanotubes using a direct current power supply. (A) Some particles that are not patterned can be seen. (B) Smaller particles condensed on the surface in no definite form.

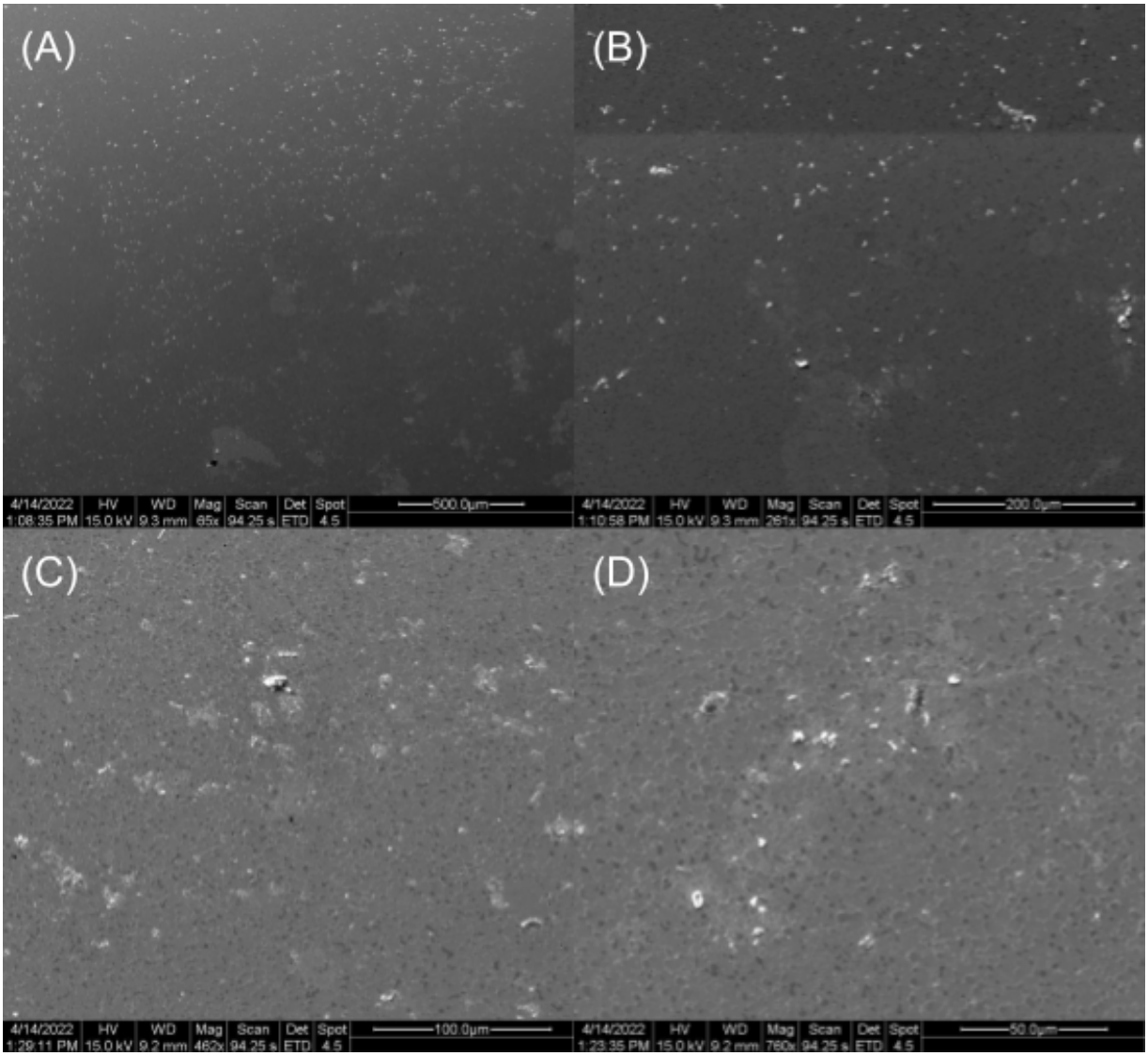

Figure 24. These micrographs are sourced from a simultaneous passivation and depositional step. Possibly oxidized arc nanotubes were suspended in the sulfuric acid electrolyte. (A) Arc nanotubes can be seen highlighted as white specs. (B) A closer magnification of these specs. (C) There seems to be a milky film encapsulating larger deposition sites. (D) The milky film becomes a gradient at higher magnifications, these may be extremely small nanoparticles. However, no distinct patterning is seen here.

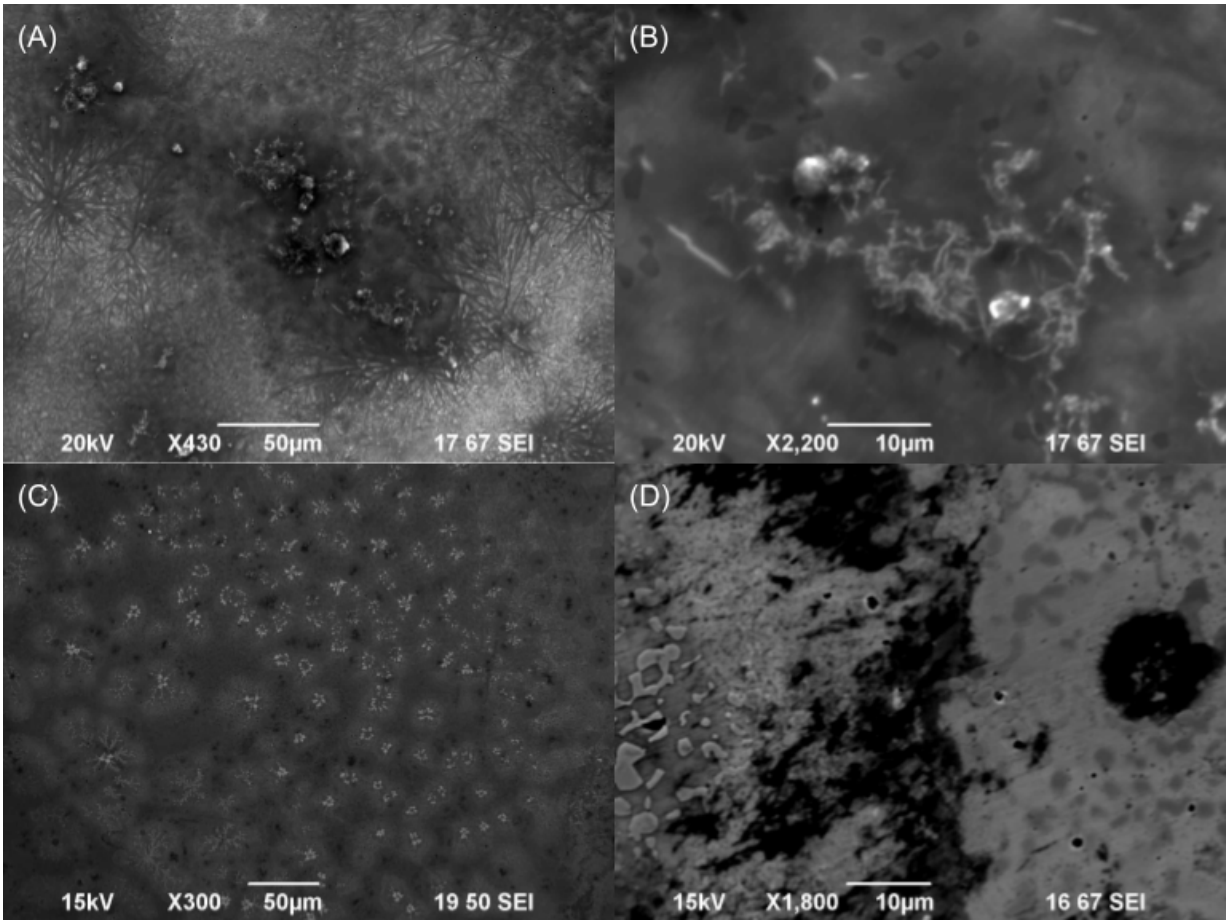

Figure 25. These depositions resulted from CVD nanotubes suspended in an acetone and sodium dodecyl sulfate solution. (A) Physical deposition forms entanglements of nanotubes. Crystalized SDS is visible at the edges of the micrograph. (B) This is a closer magnification of the nanotube entanglement. The tubular shape of these particles are pronounced. (C) A linear sweep deposition crystalized SDS at unique nucleation sites, branching out like trees. (D) A boundary of highly coagulated nanotubes separating an over passivated and regularly treated surface. The nanotubes are dark due to high conductivity and adhesion from the power pulses waveform.

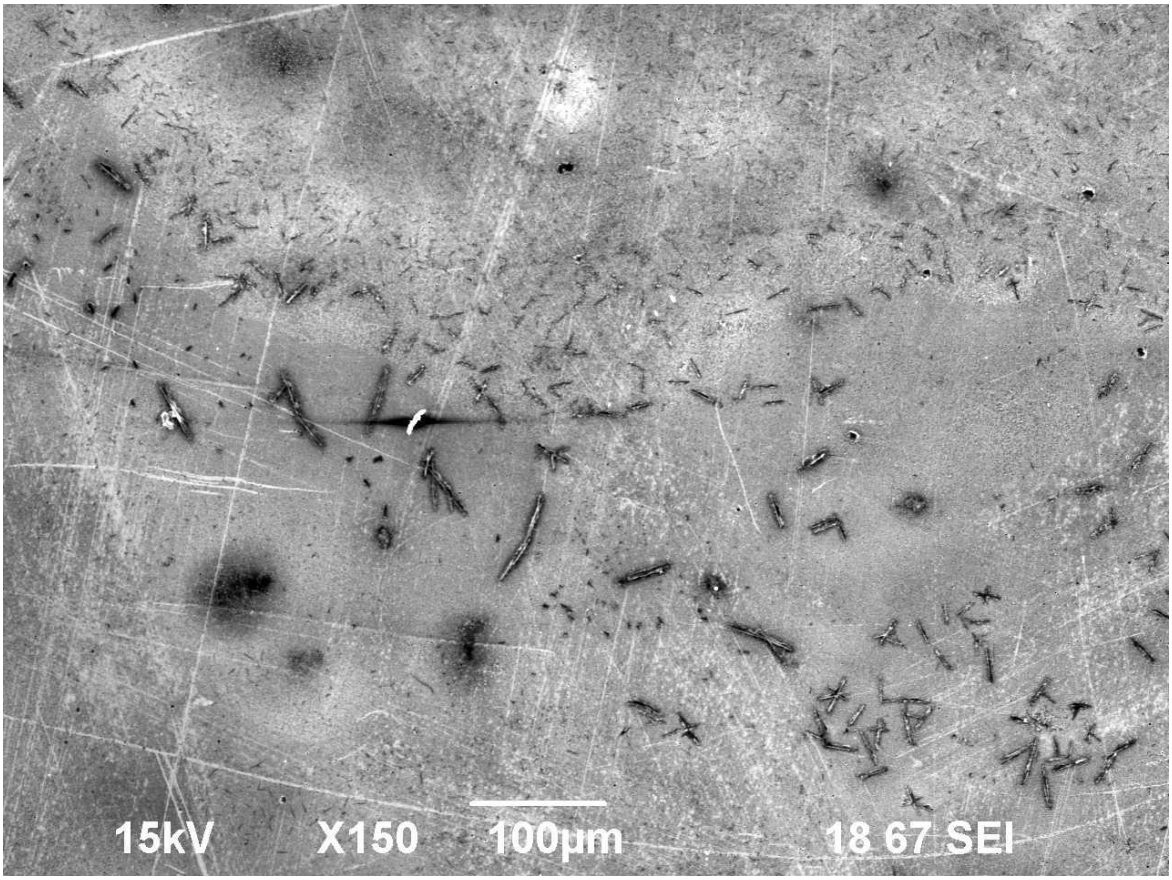

Figure 26. This micrograph depicts the effects of an applied cyclic square wave voltage on CVD nanotubes suspended in an acetone and SDS dispersion fluid. The nanotubes aggregate into large columnar formations. These formations are highly conductive and adhere well to the steel surface. Unusual contrasting methods were necessary in order to image these formations properly. A gradient can be seen in the columns ranging from 100 microns down to nanometers.

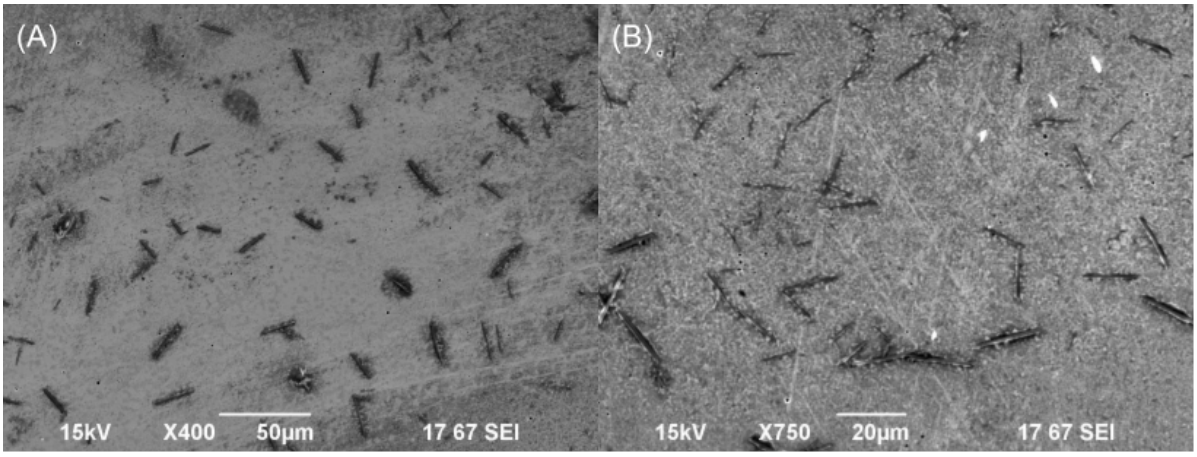

Figure 27. Above are columnar square wave CVD nanotubes at higher magnifications. (A) Most columns are evenly spread out which indicates strong dispersion. (B) Some formations are extremely small and demonstrate the impressive aspect ratio of these thin nanotubes.

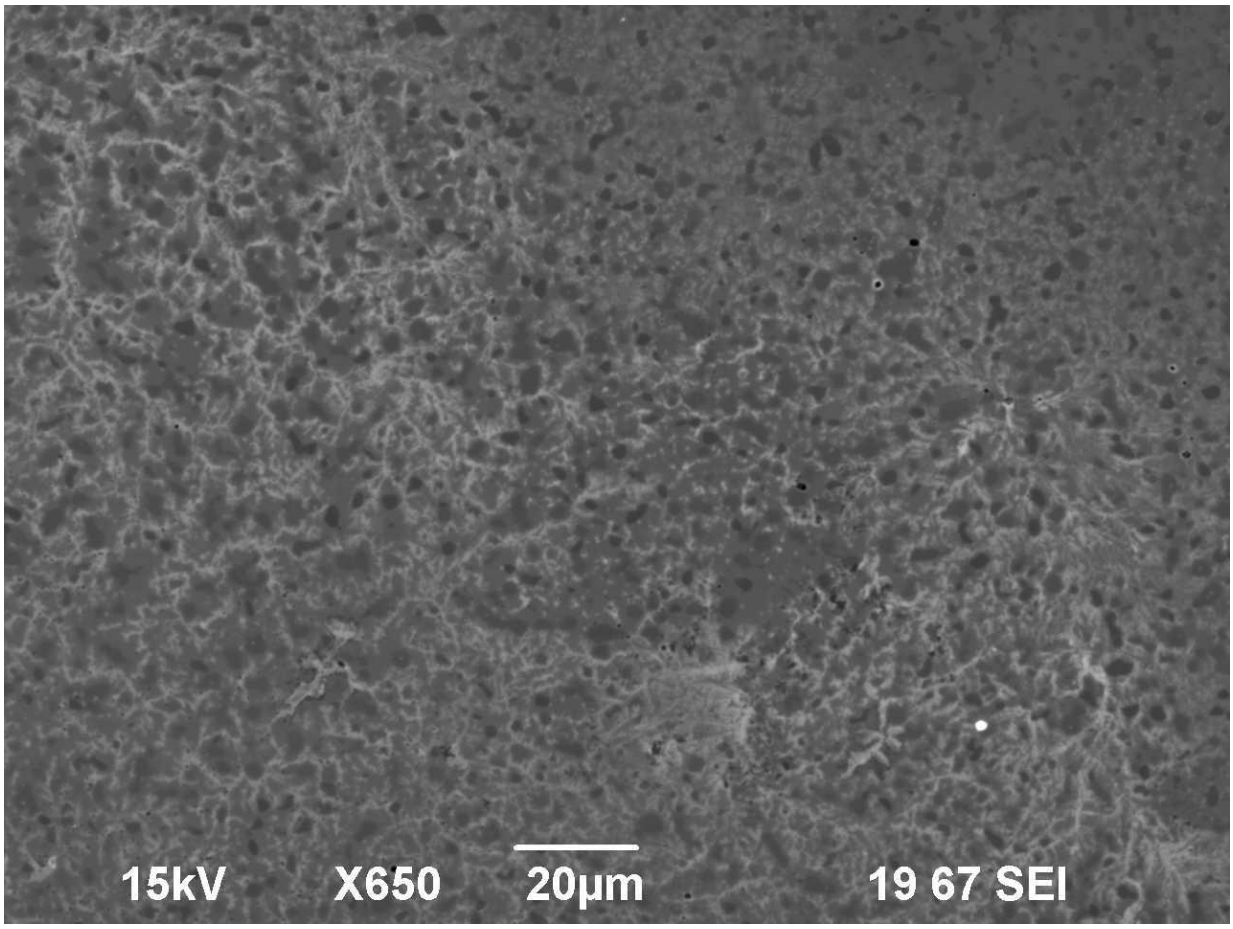

Figure 28. A constant potential step using the CVD, acetone, and SDS mixture generates impressive crystalline structures. These structures are likely to be solidified SDS, entrapping some nanotubes in the crystal matrix. The SDS crystals can clearly be seen navigating along the ferric matrix whilst avoiding chromium carbide and nitride islands. This is an unexpected yet extremely useful result as the SDS is crystallizing preferentially and can lead to future patterning. Specifically, the height difference between SDS and the chromium carbide and nitride islands may prove to be effective microfluidic filters, guiding the placement of future carbon nanotube depositions.

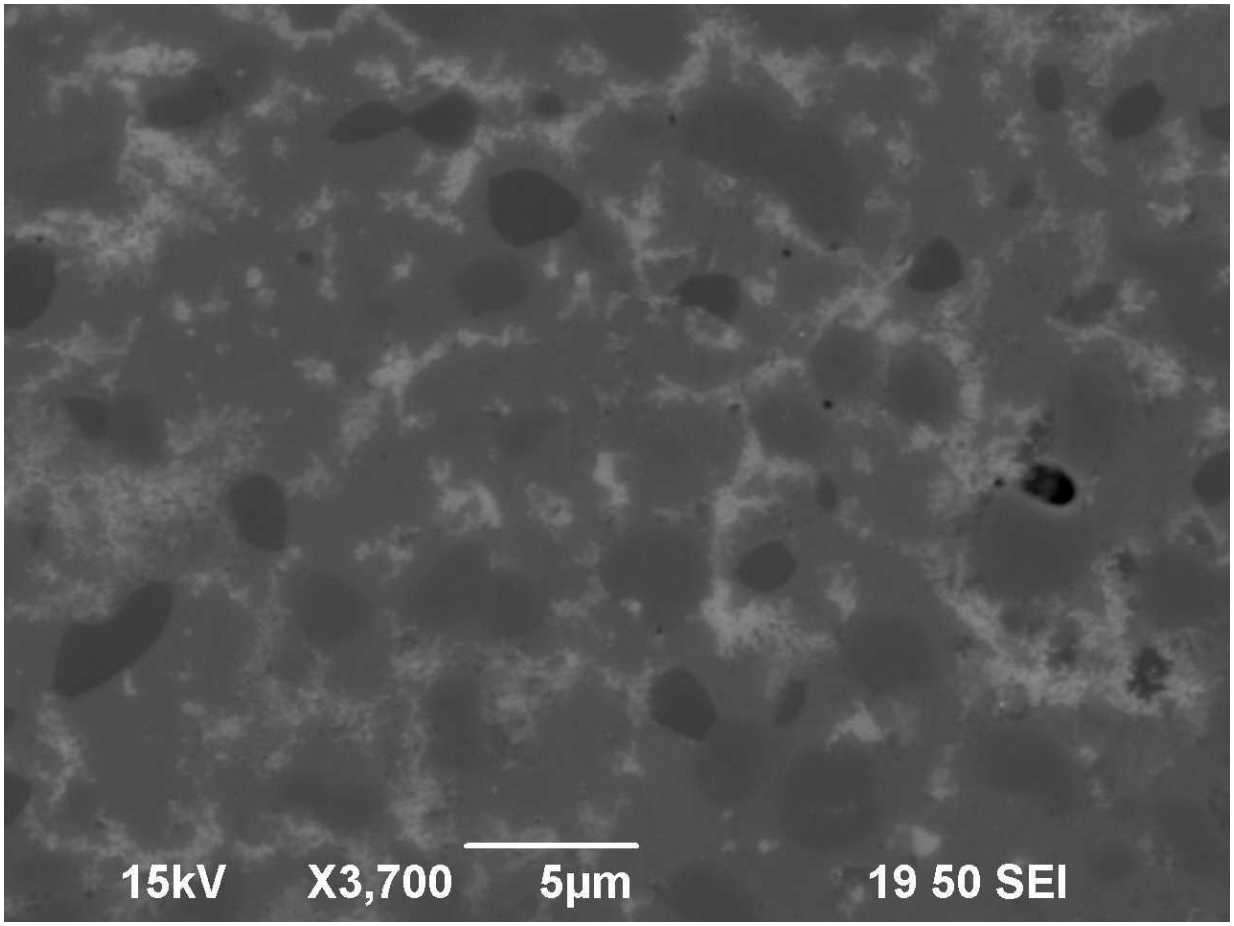

Figure 29. Overhead is a magnified image of crystallized SDS for a CVD deposition. Again the SDS coasts around the chromium carbide and nitride islands, but does not typically cut through it.

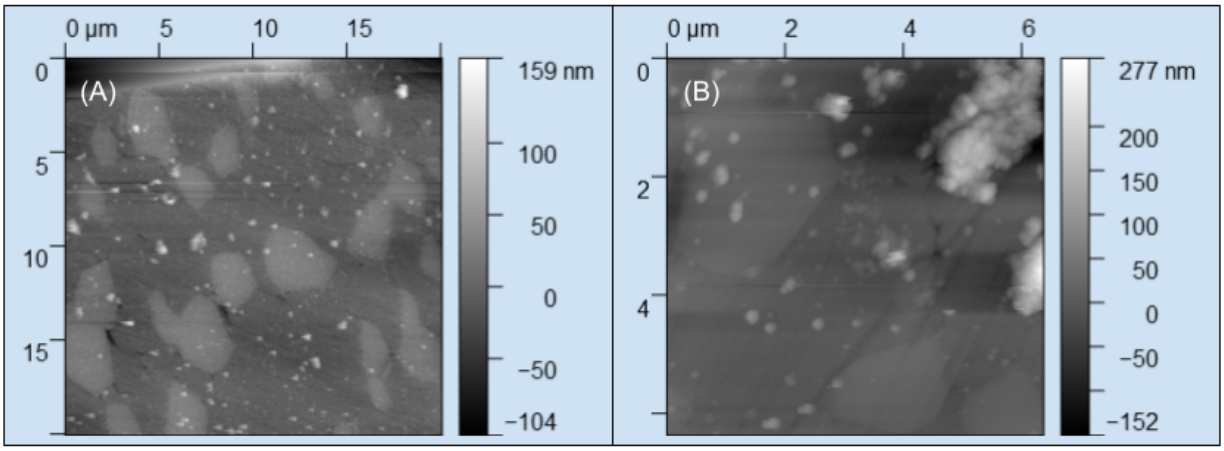

Figure 30. AFM was utilized to image the sulfuric acid arc nanotube single step linear sweep combination. (A) A height difference between the ferric matrix and the chromium carbide and nitride islands is noticeable. (B) Reasonably, carbon nanoparticles atop the steel are the tallest particles on this micrograph.

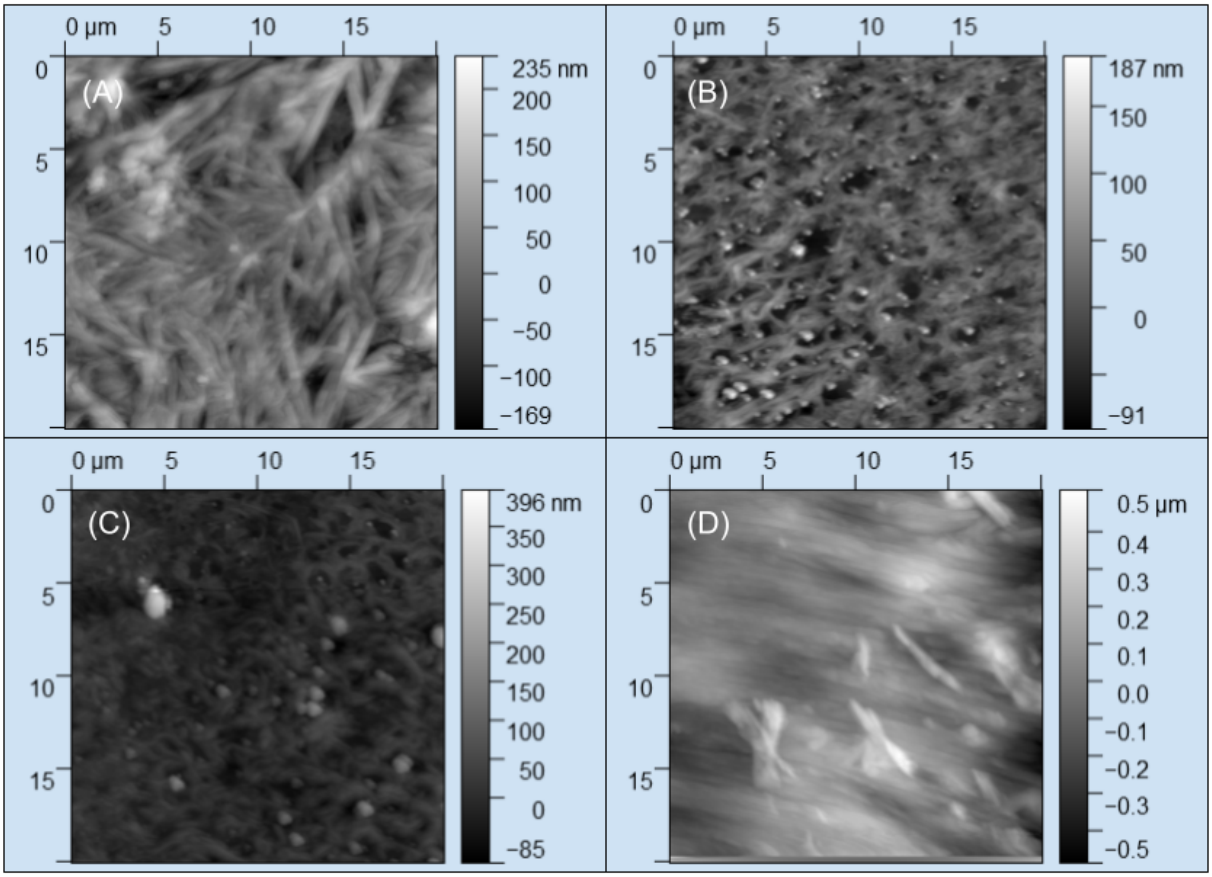

Figure 31. These atomic force micrographs analyze the surface of steel treated in a physical CVD, acetone, SDS environment. (A) A unique snowflake-like crystalline formation of SDS is visible. (B) Crystalline SDS surrounds chromium carbides and nitrides, producing a height difference. Nanoparticles fill the embankments of the carbide and nitride island SDS boundary due to microfluidics. (C) A similar process can be seen with larger nanoparticles. (D) Cross hatched nanotubes can be seen marking a variance in nanoparticle aglomerate formations.

7. Discussion

The uncharted nature of this project led to reduced statistical significance. Focus was placed on trying as many new and unique deposition techniques as possible to increase the probability of success. Extremes were tested to determine boundaries of practical deposition. For example, pitting samples and trying high CNT concentrations helped define base parameters. Results that indicate preferential deposition may have occurred under some conditions, however the majority of tests did not prove effective. Fortunately, these experiments still provide learning value.

Depositing CNTs on an untreated stainless steel surface (super polished but not passivated), resulted in no observable preference in deposition. The chromium oxide passivation layer is crucial to patterning. There is no evidence that combining the passivation electrolyte and the nanotube dispersion fluid and processing step resulted in preferential deposition either. For the mixture of sulfuric acid and arc discharge nanoparticles, some deposition is observed at the surface, however it is clumped sporadically with a thin film surrounding these coagulations, which may be smaller particles. Additionally, a fluid mixture of phosphoric acid, Tuball Battery NMP nanotubes, and dimethyl sulfoxide produced a surface littered with unorganized nanotubes contaminated with various unevaporated liquid films. Finally, the presence of CNTs in acid may have oxidized them, altering their physical or even electrical properties. Although it was important to test these methods for the sake of efficiency, they did not satisfy the overall objective of this project.

The arc discharge CNTs performed interestingly in isopropyl alcohol. When exposed to an electromagnetic field provided by the power pulses voltage setting, the nanoparticles spheroidized into micron sized orbs. These orbs appeared rather bright in the SEM, which suggest they are absorbing and retaining electrons, meaning they are less conductive. This may be due to the contaminant nanoparticles like carbon fullerenes present in the arc discharge process. It is a possibility that the variation of nanoparticles induced conductive, semiconductive, and even insulating properties. Although this discovery was not exactly what was sought after, it supported a hypothesis that applied waveform could affect nanotube deposition, in this case via geometry.

The most successful deposition environment contained pristine CVD SWCNTs in acetone and SDS. The high purity of these nanotubes may have partly attributed to their success, reducing variable properties from contaminant particles. A physical deposition of this mixture (that is dropping a single drop onto the surface and analyzing after the liquid evaporates) produced CNT entanglements. Individual threads can be seen from the micrographs alongside crystalized SDS. Applying a steady linear sweep wave form crystallized the SDS in a unique manner, similar to trees branching out of nucleation sites. Power pulses seemed to force the nanotubes to adhere rather well to the surface as they appear black in the SEM. Some spheroidized particles were also found which are somewhat congruent to the arc discharge

particles. Under a constant potential step, the SDS crystallizes in by far the most important fashion. SDS solidifies atop the stainless steel, navigation only on the ferric matrix, avoiding the chromium carbide and nitride islands that protrude from the microstructure of Nitromax. This discovery clearly shows patterning of some sort, as the height structure of the area occupying the ferric matrix is raised relative to the carbide and nitride islands. The AFM micrographs additionally present what seem to be carbon nanoparticles entrapped along the banks and edges of this crystallized SDS, which happen to be exactly where the chromium carbide and nitride island phases reside. The mechanism that drives this sort of deposition may relate to microfluidics, and the process of evaporation with respect to a mobile liquid surface boundary. Alternatively, the crystalline SDS may be relatively nonconductive compared to the island phases. The specific boundaries between the two may serve as electromagnetic field concentrators, directing CNTs out of suspension into these particular positions. This result hits the primary objective of this project. CNTs have been preferentially deposited.

Furthermore, in the presence of an electromagnetic field generated by a cyclic square wave, the CVD SWNT aggregate into columnar formations of gradient sizes ranging from 100 microns to nanometers in length. These CNT columns adhered extremely well to the stainless steel surface and were highly conductive, as they were unusually difficult to image in the scanning electron microscope. Contrast and brightness had to be altered in large amplitudes to properly outline their geometries. Unfortunately, the separation and placement of these columnar formations was random at best, indicating no real preferential deposition.

8. Conclusions and Recommendations

Overall, the objective of this project was to preferentially deposit metal nanoparticle terminated SWCNTs onto the surface of a proprietary stainless steel surface. Electrochemical passivation of Nitromax steel in sulfuric acid is necessary in order to coat the ferric matrix in an insulating chromium oxide layer surrounding chromium carbide and nitride island phases. The boundaries of these phases serve as electromagnetic field concentrators, which is the driving force behind CNT deposition. Distinct electromagnetic fields generated from various applied voltage waveforms were experimentally tested to several CNT suspensions. Depositional wave forms tested consisted of physical depositions, linear sweeps, potential steps, cyclic squares, and power pulses. Single walled metal nanoparticle terminated arc discharge CNTs were tested alongside high purity CVD CNTs and Tuball Battery NMP CNTs. Dispersion fluids and agents included water, isopropyl alcohol, acetone, dimethyl sulfoxide, and sodium dodecyl sulfate.

Altering the applied voltage waveform had a significant effect on CNT deposition and formation. Physical depositions entangled CVD nanotubes. Linear sweeps in combination with arc discharge nanotubes produced milky films around large nanoparticle deposition sites. Constant potential steps crystallized SDS in acetone to form relatively tall networks that would navigate on top of the ferric matrix avoiding chromium carbide and nitride islands. Physical

depositions with similar networks deposited CNTs at the banks of crystallized SDS, in the newly formed chromium carbide and nitride wells. This kind of patterning is what was initially targeted by the project. The mechanism driving this could be related to microfluidics and river sedimentation. CVD nanotubes in the presence of cyclic squarewaves agglomerated into highly conductive columnar formations that adhered well onto the stainless steel surface. Power pulsed electromagnetic fields resulted in spheroidized arc discharge carbon nanoparticles. Waveforms with voltages alternating between positive and negative amplitudes drastically changed the depositional geometry of carbon nanoparticle formations.

Future experimentation should prioritize working with high purity CVD SWNT in a mixture of acetone and SDS. These nanotubes were the most responsive to cyclic square waves. However, crystalline SDS can be grown under standard potential step conditions. It may prove effective to first form a crystalline SDS layer and then try a separate cyclic square wave deposition. Ideally, this would result in highly conductive columnar nanotube formations adhered to the boundaries of chromium carbide and nitride islands and the banks of crystalline SDS. Furthermore, energy dispersive spectroscopy may be utilized to identify and confirm the chemical composition of crystalline and nanoparticle formations. Electrical impedance spectroscopy may also be helpful in identifying specific nanotube deposition validities and sizes. Finally, repetition of these experiments would greatly increase statistical significance and support more robust conclusions.

9. References

[1] D. A. Gomez-Gualdrón, J. C. Burgos, J. Yu, and P. B. Balbuena, "Carbon nanotubes," Progress in Molecular Biology and Translational Science, pp. 175–245, 2011.

[2] K. A. Wepasnick, B. A. Smith, J. L. Bitter, and D. Howard Fairbrother, "Chemical and structural characterization of carbon nanotube surfaces," Analytical and Bioanalytical Chemistry, vol. 396, no. 3, pp. 1003–1014, 2010.

[3] P. Avouris, "Carbon Nanotube Electronics," Chemical Physics, vol. 281, no. 2-3, pp. 429–445, 2002.

[4] X. Zhao, Y. Ando, Y. Liu, M. Jinno, and T. Suzuki, "Carbon nanowire made of a long linear carbon chain inserted inside a multiwalled carbon nanotube," Physical Review Letters, vol. 90, no. 18, 2003.

[5] V. V. Pokropivny and V. V. Skorokhod, "New dimensionality classifications of nanostructures," Physica E: Low-dimensional Systems and Nanostructures, vol. 40, no. 7, pp. 2521–2525, 2008.

[6] "Applications of carbon nanotubes," *AZO Nano*, 23-Apr-2018. [Online]. Available: https://www.azonano.com/article.aspx?ArticleID=4842. [Accessed: 03-Jun-2022].

[7] M. Filchakova, "What are multi walled carbon nanotubes? MWCNT production, properties, and applications," Tuball, 29-Dec-2021. [Online]. Available: https://tuball.com/articles/multi-walled-carbon-nanotubes. [Accessed: 21-May-2022].

[8] A. Hemasa, N. Naumovski, W. Maher, and A. Ghanem, "Application of carbon nanotubes in chiral and achiral separations of pharmaceuticals, biologics and Chemicals," Nanomaterials, vol. 7, no. 7, p. 186, 2017.

[9] J. Doh, S.-I. Park, Q. Yang, and N. Raghavan, "The effect of carbon nanotube chirality on the electrical conductivity of polymer nanocomposites considering tunneling resistance," Nanotechnology, vol. 30, no. 46, p. 465701, 2019.

[10] Brahim Attaf, "An Eco-Approach to Boost the Sustainability of Carbon Nanotube-Based Composite Products", *Research and Innovation in Carbon Nanotube-Based Composites*, ISBN 978-0-9889190-1-3, WAP-AMSA, 2015.

[11] H. Zhang, Y. Yang, D. Ren, L. Wang, and X. He, "Graphite as anode materials: Fundamental mechanism, recent progress and advances," Energy Storage Materials, vol. 36, pp. 147–170, 2021.

[12] J. Asenbauer, T. Eisenmann, M. Kuenzel, A. Kazzazi, Z. Chen, and D. Bresser, "The success story of graphite as a lithium-ion anode material – fundamentals, remaining challenges, and recent developments including silicon (oxide) composites," Sustainable Energy & Fuels, vol. 4, no. 11, pp. 5387–5416, 2020.

[13] Susobhan Das, J. Li, and R. Hui, "Impact of Electrode Surface/Volume Ratio on Li-ion Battery Performance," ResearchGate COMSOL Conference, 2014.

[14] Z.-D. Huang, K. Zhang, T.-T. Zhang, R.-Q. Liu, X.-J. Lin, Y. Li, X.-M. Feng, Q.-B. Mei, T. Masese, Y.-W. Ma, and W. Huang, "Binder-free graphene/carbon nanotube/Silicon Hybrid Grid as freestanding anode for high capacity lithium ion batteries," Composites Part A: Applied Science and Manufacturing, vol. 84, pp. 386–392, 2016.

[15] S. Xiao, D. Pan, L. Wang, Z. Zhang, Z. Lyu, W. Dong, X. Chen, D. Zhang, W. Chen, and H. Li, "Porous cuo nanotubes/graphene with sandwich architecture as high-performance anodes for lithium-ion batteries," Nanoscale, vol. 8, no. 46, pp. 19343–19351, 2016.

[16] R. Liu, C. Shen, Y. Dong, J. Qin, Q. Wang, J. Iocozzia, S. Zhao, K. Yuan, C. Han, B. Li, and Z. Lin, "Sandwich-like CNTS/si/C nanotubes as high performance anode materials for lithium-ion batteries," Journal of Materials Chemistry A, vol. 6, no. 30, pp. 14797–14804, 2018.

[17] R. Tian, S.-H. Park, P. J. King, G. Cunningham, J. Coelho, V. Nicolosi, and J. N. Coleman, "Quantifying the factors limiting rate performance in battery electrodes," Nature News, 29-Apr-2019. [Online]. Available: https://www.nature.com/articles/s41467-019-09792-9. [Accessed: 21-May-2022].

[18] Y. Chen, X. Li, L. Zhou, Y.-W. Mai, and H. Huang, "High-performance electrospun nanostructured composite fiber anodes for lithium–ion batteries," Multifunctionality of Polymer Composites, pp. 662–689, 2015.

[19] W. Xiao, Y. Qiu, Q. Xu, J. Wang, C. Xie, J. Peng, J. Hu, J. Zhang, and X. Li, "Building sandwich-like carbon coated si@cnts composites as high-performance anode materials for lithium-ion batteries," Electrochimica Acta, vol. 364, p. 137278, 2020.

[20] S. Jessl, S. Engelke, D. Copic, J. J. Baumberg, and M. De Volder, “Anisotropic carbon nanotube structures with high aspect ratio nanopores for Li-ion battery anodes,” *ACS Applied Nano Materials*, vol. 4, no. 6, pp. 6299–6305, 2021.

[21] S. Zhang, G. Yang, X. Li, Y. Li, Z. Wang, and L. Chen, “Controlled lithium deposition,” *Frontiers in Energy Research*, vol. 10, 2022.

[22] C. Zhang, R. Lyu, W. Lv, H. Li, W. Jiang, J. Li, S. Gu, G. Zhou, Z. Huang, Y. Zhang, J. Wu, Q. H. Yang, and F. Kang, “A lightweight 3D cu nanowire network with phosphidation gradient as current collector for high‐density nucleation and stable deposition of lithium,” *Advanced Materials*, vol. 31, no. 48, p. 1904991, 2019.

[23] Y. Liu, D. Gao, H. Xiang, X. Feng, and Y. Yu, “Research progress on copper-based current collector for lithium metal batteries,” *Energy & Fuels*, vol. 35, no. 16, pp. 12921–12937, 2021.

[24] A. Corletto and J. G. Shapter, “Nanoscale patterning of carbon nanotubes: Techniques, applications, and future,” *Advanced Science*, vol. 8, no. 1, p. 2001778, 2020.

[25] R. Marani and A. G. Perri, “THE NEXT GENERATION OF FETs: CNTFETs .” Electronic Devices Laboratory, Electrical and Information Engineering Department, Polytechnic University of Bari, Bari, Italy.

[26] P. Chandrasekhar, “CNT applications in microelectronics, ‘Nanoelectronics,’ and ‘Nanobioelectronics,’” *Conducting Polymers, Fundamentals and Applications*, pp. 65–72, 2018.

[27] M. D. Bishop, G. Hills, T. Srimani, C. Lau, D. Murphy, S. Fuller, J. Humes, A. Ratkovich, M. Nelson, and M. M. Shulaker, “Fabrication of carbon nanotube field-effect transistors in commercial silicon manufacturing facilities,” *Nature Electronics*, vol. 3, no. 8, pp. 492–501, 2020.

[28] “Field-Effect Transistors,” *NanoIntegris*, 11-Oct-2017. [Online]. Available: https://nanointegris.com/applications/field-effect-transistors/. [Accessed: 03-Jun-2022].

[29] H. W. Zhu, C. L. Xu, D. H. Wu, B. Q. Wei, R. Vajtai, and P. M. Ajayan, “Direct synthesis of long single-walled carbon nanotube strands,” *Science*, vol. 296, no. 5569, pp. 884–886, 2002.

[30] R. Sharma, A. K. Sharma, and V. Sharma, “Synthesis of carbon nanotubes by arc-discharge and chemical vapor deposition method with analysis of its morphology, dispersion and functionalization characteristics,” *Cogent Engineering*, vol. 2, no. 1, p. 1094017, 2015.

[31] A. Eatemadi, H. Daraee, H. Karimkhanloo, M. Kouhi, N. Zarghami, A. Akbarzadeh, M. Abasi, Y. Hanifehpour, and S. W. Joo, "Carbon nanotubes: Properties, synthesis, purification, and medical applications," *Nanoscale Research Letters*, vol. 9, no. 1, 2014.

[32] A. Szabó, C. Perri, A. Csató, G. Giordano, D. Vuono, and J. B. Nagy, "Synthesis methods of carbon nanotubes and related materials," *Materials*, vol. 3, no. 5, pp. 3092–3140, 2010.

[33] K. Mukhopadhyay, A. Koshio, N. Tanaka, and H. Shinohara, "A simple and novel way to synthesize aligned nanotube bundles at low temperature," *Japanese Journal of Applied Physics*, vol. 37, no. Part 2, No. 10B, 1998.

[34] C. T. Kingston and B. Simard, "Fabrication of carbon nanotubes," *Analytical Letters*, vol. 36, no. 15, pp. 3119–3145, 2003.

[35] M. Ikram, A. Raza, A. Shahbaz, H. Ijaz, S. Ali, A. Haider, M. Tayyab Hussain, J. Haider, A. Ahmed Rafi, and S. Ali, "Carbon nanotubes," *21st Century Advanced Carbon Materials for Engineering Applications - A Comprehensive Handbook*, 2021.

[36] R. Brukh and S. Mitra, "Mechanism of carbon nanotube growth by CVD," *Chemical Physics Letters*, vol. 424, no. 1-3, pp. 126–132, 2006.

[37] W. Z. Li, J. G. Wen, and Z. F. Ren, "Effect of temperature on growth and structure of carbon nanotubes by chemical vapor deposition," Applied Physics A: Materials Science & Processing, vol. 74, no. 3, pp. 397–402, 2002.

[38] V. Choudhary, B. P. Singh, and R. B. Mathur, "Carbon nanotubes and their composites," *Syntheses and Applications of Carbon Nanotubes and Their Composites*, 2013.

[39] M. Zakaria and S. M. Shariff, "Factors affecting carbon nanotubes (CNTS) synthesis via the chemical vapour deposition (CVD) method," *AIP Conference Proceedings*, 2007.

[40] G. Tripathi, B. Tripathi, M. K. Sharma, Y. K. Vijay, A. Chandra, and I. P. Jain, "A comparative study of arc discharge and chemical vapor deposition synthesized carbon nanotubes," *International Journal of Hydrogen Energy*, vol. 37, no. 4, pp. 3833–3838, 2012.

[41] X. Huang, R. Farra, R. Schlögl, and M.-G. Willinger, "Growth and termination dynamics of multiwalled carbon nanotubes at near ambient pressure: An in situ transmission electron microscopy study," *Nano Letters*, vol. 19, no. 8, pp. 5380–5387, 2019.

[42] M. Hiramatsu and M. Hori, "Aligned growth of single-walled and double-walled carbon nanotube films by control of Catalyst Preparation," *Carbon Nanotubes - Synthesis, Characterization, Applications*, 2011.

[43] Y. Jiang, H. Song, and R. Xu, "Research on the dispersion of carbon nanotubes by ultrasonic oscillation, surfactant and centrifugation respectively and fiscal policies for its industrial development," *Ultrasonics Sonochemistry*, vol. 48, pp. 30–38, 2018.

[44] H. Cui, X. Yan, M. Monasterio, and F. Xing, "Effects of various surfactants on the dispersion of mwcnts–oh in aqueous solution," *Nanomaterials*, vol. 7, no. 9, p. 262, 2017.

[45] G. SUN, Z. LIU, and G. CHEN, "Dispersion of pristine multi-walled carbon nanotubes in common organic solvents," *Nano*, vol. 05, no. 02, pp. 103–109, 2010.

[46] M. Sianipar, S. H. Kim, K. Khoiruddin, F. Iskandar, and I. G. Wenten, "Functionalized carbon nanotube (CNT) membrane: Progress and challenges," *RSC Advances*, vol. 7, no. 81, pp. 51175–51198, 2017.

[47] H. Li and Y. Qiu, "Dispersion, sedimentation and aggregation of multi-walled carbon nanotubes as affected by single and binary mixed surfactants," *Royal Society Open Science*, vol. 6, no. 7, p. 190241, 2019.

[48] J. Yu, N. Grossiord, C. E. Koning, and J. Loos, "Controlling the dispersion of multi-wall carbon nanotubes in aqueous surfactant solution," *Carbon*, vol. 45, no. 3, pp. 618–623, 2007.

[49] J. Makowska, D. Wyrzykowski, B. Pilarski, and L. Chmurzyński, "Thermodynamics of sodium dodecyl sulphate (SDS) micellization in the presence of some biologically relevant ph buffers," *Journal of Thermal Analysis and Calorimetry*, vol. 121, no. 1, pp. 257–261, 2015.

[50] Z. Cai, X. Wang, W. Hong, B. Luo, Q. Zhao, and L. Li, "Grain‐size–dependent dielectric properties in nanograin ferroelectrics," *Journal of the American Ceramic Society*, vol. 101, no. 12, pp. 5487–5496, 2018.

[51] D. Fuertes Marrón, S. Sadewasser, A. Meeder, T. Glatzel, and M. C. Lux-Steiner, "Electrical Activity at Grain Boundaries of Cu(In,Ga)Se2 Thin Films," *Physical Review B*, vol. 71, no. 3, 2005.

[52] Z.-J. Wang, S. Tsurekawa, K. Ikeda, T. Sekiguchi, and T. Watanabe, "Relationship between Electrical Activity and Grain Boundary Structural Configuration in Polycrystalline Silicon," *Interface Science*, vol. 7, no. 2, pp. 197–205, 1999.

[53] "Scanning Electron Microscopy," Nanoscience Instruments, 19-Aug-2020. [Online]. Available: https://www.nanoscience.com/techniques/scanning-electron-microscopy/. [Accessed: 25-Jul-2021].

[54] “Jeol Glossary,” Jeol. [Online]. Available: https://www.jeol.co.jp/en/words/emterms/search_result.html. [Accessed: 25-Jul-2021].

[55] “Magnification,” Magnification | A Level Notes. [Online]. Available: https://alevelnotes.com/notes/biology/cells/cell-structure/magnification. [Accessed: 25-Jul-2021].

[56] “Scanning Electron Microscope - Advantages and Disadvantages in Imaging,” MicroscopeMaster. [Online]. Available: https://www.microscopemaster.com /scanning-electron-microscope.html. [Accessed: 25-Jul-2021].

[57] E. Pretorius, “Influence of acceleration voltage on scanning electron microscopy of human blood platelets,” *Microscopy Research and Technique*, 2009.

[58] “Relationship between Acceleration Voltage and Image - Electron Microscope (SEM) Technical Explanation Series (1),” *Matsusada Precision*, 2022. [Online]. Available: https://www.matsusada.com/column/sem-tech1.html. [Accessed: 03-Jun-2022].

[59] W. Li and W. Bauhofer, “Imaging of CNTS in a polymer matrix at low accelerating voltages using a sem,” *Carbon*, vol. 49, no. 12, pp. 3891–3898, 2011.

[60] A. E. Vladar, “Strategies for scanning electron microscopy sample preparation and characterization of Multiwall Carbon Nanotube Polymer Composites,” 2016.

[61] L. L. Wang, E. Heripre, S. El Outmani, D. Caldemaison, and M. Bornert, “A simple experimental procedure to quantify image noise in the context of strain measurements at the microscale using DIC and Sem Images,” *EPJ Web of Conferences*, vol. 6, p. 40008, 2010.

[62] D. Li, J. Zhang, Y. He, Y. Qin, Y. Wei, P. Liu, L. Zhang, J. Wang, Q. Li, S. Fan, and K. Jiang, “Scanning electron microscopy imaging of single-walled carbon nanotubes on substrates,” *Nano Research*, vol. 10, no. 5, pp. 1804–1818, 2017.

[63] “Central Microscopy Research Facility,” *Scanning Electron Microscopy | Central Microscopy Research Facility*. [Online]. Available: https://cmrf.research.uiowa.edu/scanning-electron-microscopy. [Accessed: 03-Jun-2022].

[64] “Scanning electron microscopy / energy dispersive spectroscopy,” *University of Melbourne Faculty of Arts*. [Online]. Available: https://arts.unimelb.edu.au/grimwade-centre-for-cultural-materials-conservation/conservation

-services/services-support/technical-analysis/scanning-electron-microscopyenergy-dispersive-spectroscopy. [Accessed: 03-Jun-2022].

[65] S. T. Kasas, “Biological applications of the AFM: From single molecules to organs, international journal of Imaging Systems and Technology,” DeepDyve, 01-Jan-1997. [Online]. Available: https://www.deepdyve.com/lp/wiley/biological-applications-of-the-afm-from-single-molecules-to-organs-DbF0KqSe8a. [Accessed: 27-Feb-2022].

[66] M. Power, “(New Year's) resolution of an AFM probe,” NuNano AFM Probes, 14-Dec-2021. [Online]. Available: https://www.nunano.com/blog/2018/12/11/new-years-resolution-of-an-afm-probe. [Accessed: 11-Mar-2022].

[67] “What is AFM? learn about atomic force microscopy!,” NanoAndMore. [Online]. Available: https://www.nanoandmore.com/what-is-atomic-force-microscopy. [Accessed: 27-Feb-2022].

[68] Department of Materials Science and Metallurgy - University of Cambridge, “AFM Modes of Operation,” University of Cambridge. [Online]. Available: https://www.doitpoms.ac.uk/tlplib/afm/modes_operation.php. [Accessed: 27-Feb-2022].

[69] Department of Materials Science and Metallurgy - University of Cambridge, “Modes of operation,” University of Cambridge. [Online]. Available: https://www.doitpoms.ac.uk/tlplib/afm/modes_operation.php. [Accessed: 17-Mar-2022].

[70] “What is AFM?,” NanoAndMore. [Online]. Available: https://www.nanoandmore.com/what-is-atomic-force-microscopy. [Accessed: 17-Mar-2022].

[71] K. H. Choi, J. P. Bourgoin, S. Auvray, D. Esteve, G. S. Duesberg, S. Roth, and M. Burghard, “Controlled deposition of carbon nanotubes on a patterned substrate,” *Surface Science*, vol. 462, no. 1-3, pp. 195–202, 2000.

[72] J. Liu, M. J. Casavant, M. Cox, D. A. Walters, P. Boul, W. Lu, A. J. Rimberg, K. A. Smith, D. T. Colbert, and R. E. Smalley, “Controlled deposition of individual single-walled carbon nanotubes on chemically functionalized templates,” *Chemical Physics Letters*, vol. 303, no. 1-2, pp. 125–129, 1999.

[73] H. Zhou, T. Wang, and Y. Y. Duan, “A simple method for amino-functionalization of carbon nanotubes and electrodeposition to modify neural microelectrodes,” *Journal of Electroanalytical Chemistry*, vol. 688, pp. 69–75, 2013.

[74] M. Atiq Ur Rehman, Q. Chen, A. Braem, M. S. Shaffer, and A. R. Boccaccini, “Electrophoretic deposition of carbon nanotubes: Recent progress and remaining challenges,” *International Materials Reviews*, vol. 66, no. 8, pp. 533–562, 2020.

[75] “Center for Composite Materials - University of Delaware,” *CCM Alternative Current Electrophoretic Deposition of Functionalized Carbon Nanotubes Comments*. [Online]. Available: https://www.ccm.udel.edu/research_summaries/alternative-current-electrophoretic-deposition-of-functionalized-carbon-nanotubes/. [Accessed: 03-Jun-2022].

[76] S. Maulik, S. Basu, H.-C. Hou, and T. Daniels-Race, “Voltage-controlled deposition of dispersed carbon nanotubes onto a conducting substrate without a catalyst,” *Advanced Science, Engineering and Medicine*, vol. 10, no. 6, pp. 564–567, 2018.

[77] American Society for Testing and Materials, “ASTM A380/A380M Standard Practice for Cleaning, Descaling and Passivation of Stainless Steel Parts, Equipment, and Systems,” ASTM Special Technical Publication. 2021
.

[78] American Society for Testing and Materials, “ASTM A967/A967M - 17 Standard specification for chemical passivation treatments for stainless steel,” ASTM Stand., no. March, 2017.

[79] American Society for Testing and Materials, “ASTM G5 Standard Reference Test Method for Making Potentiodynamic Anodic Polarization Measurements,” Annu. B. ASTM Stand., 2014.